Chapter 8
Microstructural Effects in Hydrogen Embrittlement of Steel

The preceding two chapters describe elementary features characterizing hydrogen embrittlement (HE) of steel. HE of steel is susceptible to microstructures, and understanding of functions of microstructural factors is indispensable to proper designs against environmental degradation. Many studies have been conducted, and early works on material and environmental factors are in a review by Moody et al. for iron-base alloys [1]. Effects of alloying elements focusing on trapping of hydrogen were reviewed by Bernstein and Pressouyre [2].

It should be noted that a procedure to control a specific microstructural factor occasionally affects other factors, and separating each factor's contributions is not straightforward. For example, the grain refinement conducted by recrystallizing cold-worked iron accompanies the recovery of substructures during annealing. Also, the effects of material factors depend on environmental and mechanistic conditions. Comparisons of susceptibilities to HE of different materials must be made under proper conditions.

Functions of microstructural factors in HE manifest not only in mechanical properties but also in features such as fracture morphology, strain localization, and damage accumulation. Interactions of hydrogen with lattice defects in processes preceding the final fracture influence the final degradation. Accordingly, functions of microstructural factors must be examined throughout the entire process leading to fracture. However, studies in this context are limited in the literature. Early studies were rather phenomenological, as a matter of course, lacking modern microscopic information. In this section, the stability of substructures against external stress in the presence of hydrogen is paid particular attention to the effects of microstructural factors. It is to be noticed that the mechanism or function of hydrogen presented in each case is a subject revisited with caution.

8.1 Martensitic and Bainitic Steel

8.1.1 Tempering of Martensite and Bainite

The microstructure of lath martensitic steel is shown in Fig. 8.1 using an electron back scattering diffraction (EBSD) orientation map and a schematic illustration of structural units [3]. A prior austenite grain consists of several packets, each of which is an assembles of laths of the same habit planes. A packet consists of blocks, each of which is an assembly of laths of the same variants. Tempered martensite is the most common microstructure of high-strength steel. On tempering, internal stress is relieved by rearranging a high density of dislocations to stable structures and by precipitation of supersaturated solute carbon to carbides. Then, two main aspects are on the effects of tempering, one is substructures, and the other is precipitates morphologies.

Effects of tempering temperatures on Stage II crack growth rates and fractographic features in fracture mechanics tests are described in Sects. 6.2.2.2 and 7.2.4, respectively, for hydrogen-precharged AISI 4340 steel. An increase in tempering temperatures from 503 to 723 K reduced the yield strength from 1620 to 1340 MPa and Stage II crack growth rates. Fractographic features changed from mixtures of intergranular (IG) and quasi-cleavage (QC) to alternate IG and multiple void coalescence (MVC) regions with 100–200 μm intervals. Gerberich et al. assumed that different brittle fracture initiation sites between the two tempering conditions determine the Stage II crack growth rate [4]. Martensite lath intersections with prior austenite grain boundaries or oxysulfides are the proposed fracture initiation sites for the high- and low-strength steel.

Elevated tempering temperatures generally stabilize substructures and reduce the strength of martensite. Effects of tempering temperature are shown in Fig. 8.2 for the threshold stress intensity, K_{ISCC}, at delayed fracture tests of 0.35C–Cr–Mo steel (SCM435 in Japanese Industrial Standard) [5]. The steel was additionally alloyed
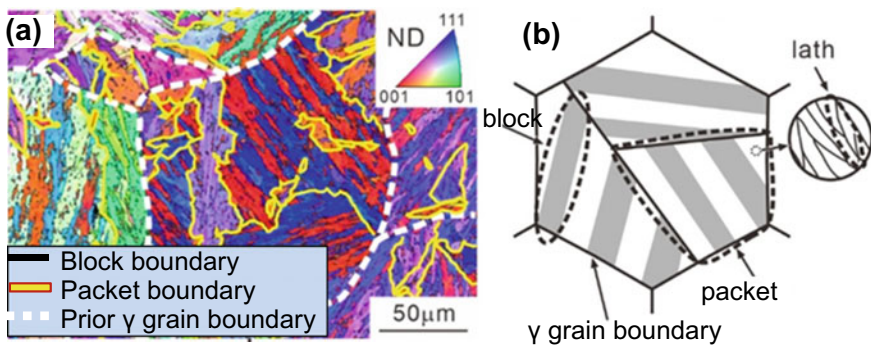

Fig. 8.1 Structures of acicular martensitic steel. (a) Electron Back Scattering Diffraction orientation map and (b) schematic illustration of structural units (Shibata et al. [3])

Fig. 8.2 Dependence of K_{ISCC} on tempering temperatures for medium-carbon Cr–Mo martensitic steels. A 0.04Nb, B 0.04Ti + 0.10 V or C 0.10 V + 0.04Nb (mass%) to the base compositions (Owada et al. [5]. Reprinted with permission from The Iron and Steel Institute, Japan)
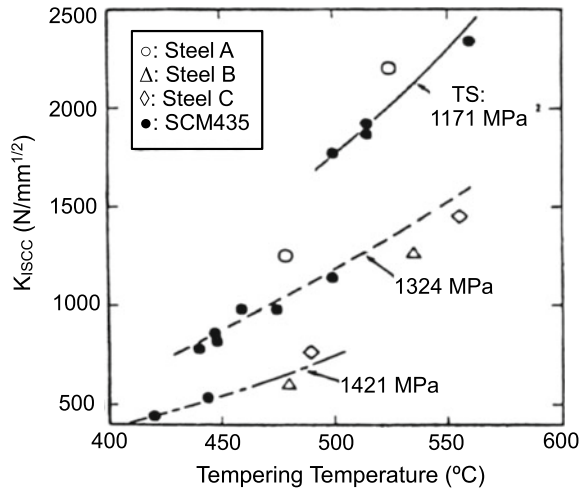

with (A) 0.04Nb, (B) 0.04Ti + 0.10 V or (C) 0.10 V + 0.04Nb (mass%) to the base compositions to control the strength level at a given tempering temperature. The delayed fracture test was a cantilever beam bend test in 3% NaCl aqueous solution using fatigue-notched specimens. Figure 8.2 separates the effect of tempering temperature on K_{ISCC} from tensile strength, classifying K_{ISCC} data into three levels in tensile strength. Lower tensile strengths obtained by higher tempering temperatures generally elevate the K_{ISCC} level, i.e., reduce the susceptibility to HE, but higher tempering temperatures increase K_{ISCC} even at a constant strength level. The ratio of K_{ISCC} to the separately measured fracture toughness K_I under non-corrosive environment was 0.45 ~ 0.15 at a given tensile strength [5].

A proper alloy design makes it possible to keep a high-strength level while elevating tempering temperature, as shown for Mo-V martensitic steel concerning reduced stress relaxation, Fig. 5.5 in Sect. 5.3.1. Secondary hardening due to the precipitation of VC at tempering of vanadium-bearing martensitic steel enables to raise tempering temperature, keeping the same strength. Improvement in the susceptibility to sustained-loading delayed fracture by the precipitation of VC is shown in Fig. 6.28 [6] for a 0.37C-0.6Si-1.0Mo-0.5Cr-0.54 V (mass%) martensitic steel tempered at 823 and 923 K. The precipitation of VC reduced the stress-relaxation rate and its enhancement by hydrogen, as shown in Fig. 5.5 [6]. Fine VC precipitates are likely to act as barriers to the motion of dislocations and their slip extension, coupled with more stabilized structures of martensite by tempering at a higher temperature.

Stabilized substructures by elevating tempering temperature reduce internal strain as observed by a linear decrease in the broadening of X-ray diffraction line width [5]. Figure 8.3 [5] shows good correlations between K_{ISCC} and internal strain estimated from the half-width of the X-ray diffraction line for the steels in Fig. 8.2. The results strongly suggest internal strain or associated dislocation arrangement is a crucial factor controlling the susceptibility to HE of martensitic steels.
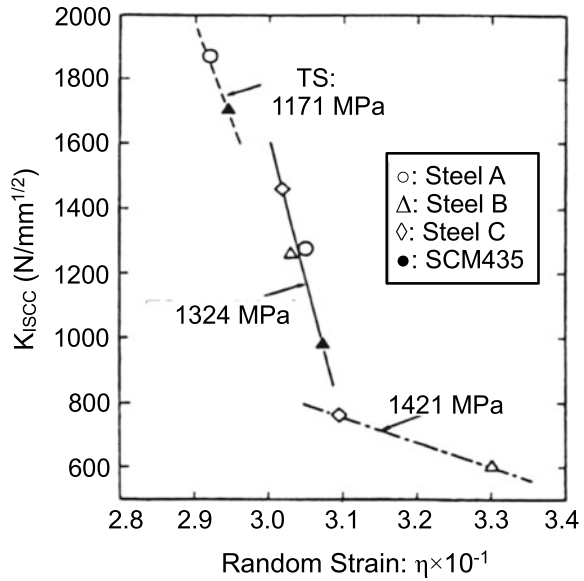
Bainite is a generic term for intermediate microstructures between pearlite and martensite reactions at the austenite decomposition [7]. The apparent structures widely vary according to transformation temperatures. Lower bainite that forms between 323 and 673 K is composed of fine ferrite plates with morphology close to martensite plates. Fe_3C and ε iron-carbide precipitate within the ferrite plates, and the dislocation density is high. The strength of lower bainite is high, but the structures are more stable than as-quenched martensite.

Comparisons of the time to fracture at delayed fracture tests for tempered martensitic and lower bainitic steels are shown in Fig. 8.4 [8]. The steels are medium carbon low-alloy steel of various compositions, and some are further micro-alloyed with V, Nb, and Ti. Isothermal transformation at 593 K or oil-quenching from austenitizing at 1273 K was given to produce bainite or martensite structures, respectively. Tempering temperatures were 873 or 773 K for the respective structure. Delayed fracture tests in Fig. 8.4 were by three-point bending at a constant strain under an applied load of 1000 MPa in 0.1 N HCl at 285 K, using circumferentially V-notched round bar specimens of 10 mm in diameter. Superior resistance to delayed fracture of lower bainite compared with martensite is evident.

The crack growth in martensitic and bainitic steel was also measured using an electric potential method at a sustained-loading four-point bending test with U-notched rectangular bar shape specimens [8]. Specimens of the two structures were 1500 MPa in tensile strength, and the initially applied stress intensity was 1500 MPa·$m^{1/2}$ in 0.1 N HCl at 285 K. The incubation time to initiate cracking was 105 and 55 min for bainite and martensite, respectively, and the crack growth rate was about one order of magnitude slower for bainite than martensite. Further, K_{ISCC}, defined as the threshold stress intensity at which a growing crack was arrested, was measured

Fig. 8.4 Relationship between tensile strength and time to fracture at nominal bending stress of 1000 MPa in three-point bending delayed fracture test in 0.1 N HCl solution (Nakasato et al. [8])
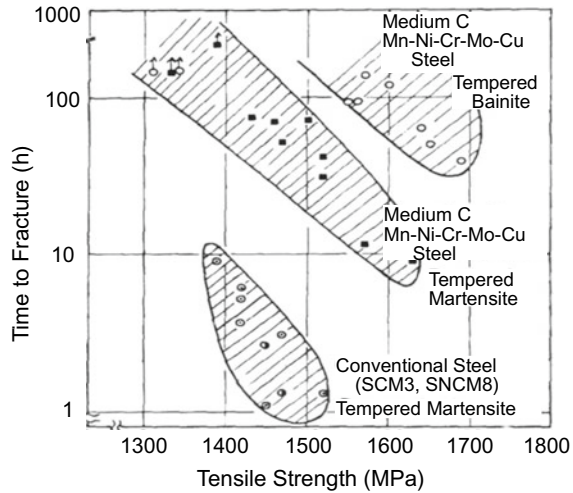
using a constant-strain wedge opening loading test in 0.1 N HCl at 285 K or in distilled water at 323 K. In that test method, stress intensity decreased with the crack extension, and K_{ISCC} of the two structures were almost the same irrespective of test solutions.

A highly supersaturated solute carbon precipitates cementite on tempering, and cementite acts as void nucleation sites on tensile deformation, as observed for spheroidized carbon steel [9], even at low hydrogen fugacity [10]. In the experiment cited above [8], precipitation of cementite along prior austenite grain boundaries was substantial in martensitic structures, and IG fracture was dominant. On the other hand, the cementite precipitation within lath was dominant in bainite structures, and the fracture surface showed QC. The lower crack growth rate in bainitic structures might be ascribed to the cementite morphology. However, some fractions of IG existed for bainite depending on the stress intensity level. The IG fracture mode was dominant for bainitic structures at applied stress levels near K_{ISCC}. Effects of cementite morphology on delayed fracture may depend on stress states and deformation stages.

Microstructural alterations caused by tempering martensitic steel are diverse, such as stabilization of dislocation structures, generation of fine precipitates, impurity segregation in grain boundaries, alteration of the strength level, and so on. Which of them is primary in interactions with hydrogen to cause premature fracture must be carefully examined.

8.1.2 Precipitates

Most martensitic steel micro-alloyed with Ti, Nb, and V contains uniformly distributed fine carbides and/or nitrides. The precipitates are associated with coherent

strain around the particles in the early stage of precipitation and act as obstacles for dislocation motion, retarding the decomposition of martensite and causing secondary hardening. Interactions of hydrogen with the precipitates increase the hydrogen absorption capacity of steel and reduce hydrogen diffusivity. Morphologies of precipitates are strongly dependent on tempering temperatures, and their function in HE is complicated depending on the situation.

Effects of V and Ti and additional Mo on sulfide stress cracking (SSC) were examined for 0.4C-1Cr-0.2Mo (mass%) martensitic steel in sustained-loading delayed fracture tests in the NACE solution (5% NaCl+ 0.5% glacial acetic acid saturated with H_2S, pH = 3) [11]. Tempering temperatures of two levels were chosen to give tensile strength in 900/950 and 1000/1050 MPa. Micro-autoradiography revealed fine precipitates, ≤ 20 nm in size.

The SSC resistance in terms of the no-failure threshold stress for all the modified steel was higher than the reference steel, which did not contain micro-alloying elements. Tempering temperatures for the two tensile strength levels were between 923 and 983 K, and the best combination of alloying elements for the threshold stress was 0.1 V-0.1Ti-0.8Mo at the tensile strength of 1000 MPa. Concentrations of weakly trapped diffusive hydrogen and diffusivities of hydrogen were also measured, but their differences among various combinations were slight, and no systematic correlations with the threshold stress were found.

Charbonnier et al. postulated that the strong hydrogen trapping potentiality of fine carbides was beneficial for the SSC resistance [11]. Their experiments measured hydrogen concentration and diffusivity using permeation and vacuum desorption methods without applying external stress. Accordingly, the trapped states of hydrogen might differ from those in stressed specimens in delayed fracture tests. The tensile strengths of specimens were the same at 1000 MPa, but different tempering temperatures, 973 K for the 0.1 V-0.1Ti-0.8Mo steel and 933 K for another steel, might have stabilized substructures, affecting the SCC susceptibility.

The superior resistance to delayed fracture in long-term atmospheric exposure was reported for vanadium-bearing martensitic steels tempered at high temperatures [12]. Steels of various compositions ranging from 1100 to 1630 MPa in tensile strength were exposed at the seaside for up to one year under external stressing. The specimens were circumferentially notched round bars, and the applied external stress was at the yield strengths. The fracture ratio, i.e., the number of failed specimens against the total 60 specimens, was used to measure the susceptibility. The best without failure was a 0.4C-1.2Cr-0.58Mo-0.35 V (mass%) steel tempered at 863 K giving 1450 MPa in tensile strength.

However, the effects of vanadium were sensitive to tempering temperatures. For V-bearing steel of 0.3C-1Si-2Cr-0.4Mo-0.35 V (mass%), the fractions of failed specimens were 6.7% and 63% for the tensile strengths of 1537 and 1627 MPa by tempering at 783 and 703 K, respectively. Delayed fracture did not occur for an Al-treated 0.2C-0.76Mn-0.64Cr (mass%) martensitic steel tempered at 623 and 713 K to the tensile strength of 1303 MPa and 1078 MPa, respectively. The above results by Yamazaki et al. were a part of studies to assess the susceptibility to delayed fracture, described in Sect. 6.4.4b.

Thermal desorption profiles of hydrogen introduced to the Mo-V steel tempered at different temperatures are shown in Fig. 3.17, indicating that VC acts as strong trap sites. Hydrogen was the tracer of defects, and Fig. 8.5 [6] shows the amounts of tracer-hydrogen recharged to specimens subjected to sustained loading under simultaneous hydrogen charging. Three conditions of specimens, i.e., (a) original without loading, (b) loaded for 8 h at 0.4 of the tensile strength, and (c) subsequently annealed at 473 K, are compared. The open and filled bars in Fig. 8.5 denote measurements after 15 min or 24 h from hydrogen charging, respectively. The difference between the open and filled bars shows the amount of diffusive tracer-hydrogen at room temperature.

Figure 8.5 indicates that applying external stress in the presence of VC enhances the creation of not only weak but also strong trap sites that remain at annealing at 473 K. The two tempering temperatures hardly affected the total amounts of diffusive hydrogen, against the presumption that the amount of diffusive hydrogen is decisive to the susceptibility. Comparing loaded and annealed conditions for specimens tempered at 923 K (650 °C) implies that the trap sites of diffusive hydrogen are mostly vacancies because annealing almost annihilated the trap sites. The amounts of diffusive hydrogen are similar between the two annealing temperatures, but the fraction of vacancies is much less in the VC-containing steel.

Limitations of using hydrogen concentration are noteworthy in assessing the susceptibility to hydrogen embrittlement. The observed total or the average hydrogen concentration per unit volume is not always a measure of the susceptibility to HE,
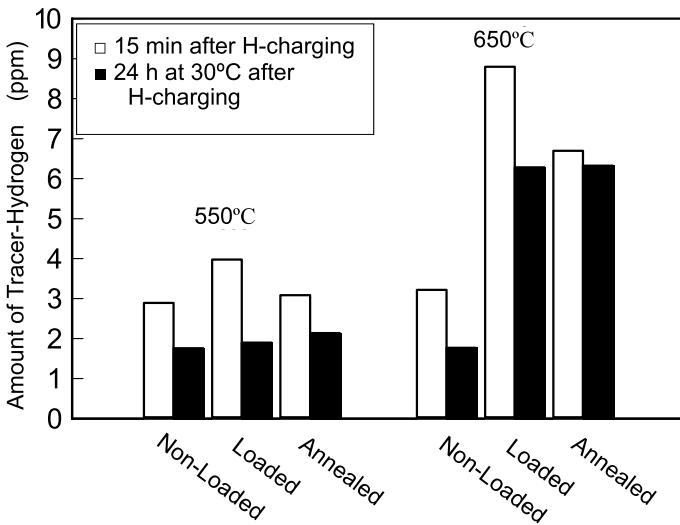

Fig. 8.5 The amounts of tracer-hydrogen introduced to three states of martensitic Mo-V steels tempered at 550 (823 K) and 650°C (923 K). (1) Non-loaded, (2) Subjected to delayed fracture tests at 0.4 of the tensile strength, (3) Annealed at 200°C after delayed fracture tests. □: Measured after 15 min after H-charging, ■: Measured after keeping at 30°C (303 K) for 24 h. M. Nagumo et al. (2003) [6]

since local plastic deformation and, thus, local trapped states of hydrogen are crucial for fracture. As observed, a uniform and dense distribution of VC particles should increase the total hydrogen absorption capacity, but a uniform distribution of VC may reduce strain localization and, thus, the local density of induced lattice defects. Such strain dispersion, rather than hydrogen itself, might be the cause of reducing the susceptibility.

Details of structural alterations during straining associated with fine precipitates are not definite. Some stress-induced alterations of dislocation arrangements around the precipitates are possible origins of forming strong trap sites and stabilizing dislocation arrangements, reducing the stress-relaxation rates. Tsuchida et al. conducted transmission electron microscopic observations of martensitic vanadium-bearing steel during tempering, referring to hydrogen absorption behaviors [13]. Effects of precipitates, in many cases, overlap those of stabilized microstructures by tempering that generates precipitates.
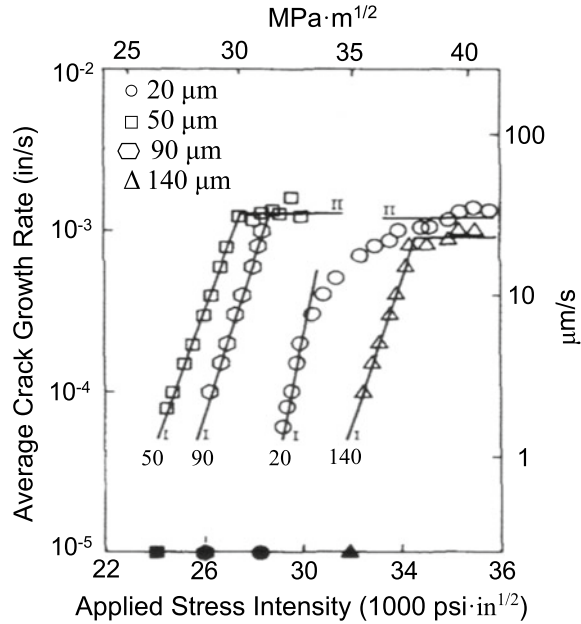
8.1.3 Grain-Size Effects

The term "grain size" in martensitic steel usually addresses prior austenite grain. The austenitizing temperature is often a controlling variable of grain size, but it accompanies compositional alterations of solute elements, including impurities present in grain boundaries. The apparent effects of grain size on HE in the literature must be carefully examined concerning other contributions like alterations of martensite substructures associated with experimental procedures such as solutionizing or annealing after cold working.

(a) Fracture mechanics tests

Grain-size effects have been evaluated in fracture mechanics tests about the crack growth rate and the threshold stress intensity K_{TH} at the onset of cracking. Hydrogen effects on crack growth are described in Sect. 6.2.2. An early study by Lessar and Gerbrich for AISI 4340 steel was on grain-size effects on K_{TH}, yield strength, and crack velocity [14]. In the experiments, the prior austenite grain size was controlled from 20 to 140 μm by varying austenitizing temperatures and holding times. Austenitizing at 1173 K for 1 h and 1373 K for 16 h also altered the tensile strength of the steel from 1460 to 1230 MPa. The tempering temperature was 573 K for all specimens. The crack length and the applied stress intensity were calculated from the load versus time record of V-notched double cantilever bend (DCB) specimens under a constant displacement. Hydrogen was precharged by cathodic electrolysis in a poisoned 4 wt.% H_2SO_4 solution at a current density of $60 A/m^2$ and was then enclosed by Cd-plating.

Figure 8.6 [14] shows Stage I and II crack growth rates of steel of various grain sizes as a function of the applied stress intensity. The test was a K-decreasing type with crack growth, and the results were complicated. Separately conducted plots showed inversely proportional Stage I crack growth rates at 33 MPa·m$^{1/2}$ to the square of

Fig. 8.6 Stage I crack growth rates at DCB tests for hydrogen-precharged AISI 4340 steels of various grain sizes (Lessar et al. [14])

the grain size. On the other hand, K_{TH} increased with the increasing grain size. The grain-size effects were associated with fracture morphologies. The primary failure mode for all grain sizes was IG, but the smaller grain size, in general, displayed a more significant amount of tear mode failure. Increasing grain size raised K_{TH}, but the net increase in K_{TH} was slight since grain coarsening concomitantly decreased the yield stress. Lessar et al. noticed that the grain size primarily affected the growth rate rather than K_{TH} and suggested that the crack growth kinetics were affected mainly by hydrogen diffusion. When the grain size was significantly large, exceeding the plastic zone size, the increased grain size improved resistance. In the crack growth, the existence of grain boundaries in the crack front plastic zone must be crucial

Grain-size effects with constant yield strength were investigated for fcc superalloy IN903 [15]. Varying solution temperatures obtained grain sizes ranging from 23 to 172 μm, and double aging controlled the yield strength, independent of grain size. Slow crack growth was measured using bolt-loaded wedge opening loading (WOL) specimens at 298 K in 207 MPa hydrogen gas. The crack growth threshold K_{TH} increased slightly but proportionately to the square root of the grain size. Comparing data for AISI 4340 and IN 903, Moody et al. concluded that grain-size effects on K_{TH} were the same for the two alloys when IG fracture prevailed [15].

In martensitic steel, impurities substantially affect fracture toughness. Effects of grain size and P-doping on the crack growth rate and the threshold stress intensity K_{TH} for the crack initiation were examined for a 0.3C-3.5Ni-1.7Cr (mass%) martensitic steel of the same yield strength of 1275 MPa, [16]. Austenite grain sizes were varied in the range of 35–450 μm by adjusting austenitizing temperatures. Compact tension

(CT) tests were conducted using specimens hydrogen precharged in hydrogen gas at 573 K, giving the hydrogen concentration of 1.2×10^{-4} in atomic ratio. For the undoped steel, the larger grain size brought about a lower growth rate and nearly the same K_{TH}. On the contrary, for the 0.06% P-doped steel, the larger grain size brought the higher stage II crack growth rate and the lower K_{TH}. The grain-size effect on Stage II crack growth rate was opposite in the P-doped and undoped steels of the same yield strength.

A high-purity AISI 4340-Type steel ($P = 0.003\%$) exhibited a substantial reduction in K_{TH} with increasing prior austenite grain size when tested in hydrogen gas using bolt-loaded modified wedge opening loading (WOL) specimens at fixed displacement [17]. Hydrogen gas pressure was about 0.1 MPa at room temperature. The magnitudes of K_{TH} in the high-purity steel were five to six times as large as that for commercial steel tested under the same condition, and the fracture mode was mainly transgranular. Banerji et al. considered that high K_{TH} with the transgranular fracture is the intrinsic effect of hydrogen in this steel and that the low K_{TH} with IG fracture was the effect of impurity such as P. Banerji et al. suggested that the austenite grain refinement should be useful as a means to increase the resistance to hydrogen-assisted cracking for high-purity steel.

(b)   Delayed fracture and tensile tests

Refinement of the prior austenite grain size improved the resistance against sulfide stress cracking (SSC) in martensitic steel of 600 to 850 MPa in yield strength [18]. At constant load delayed fracture tests in a 0.5% CH_3COOH+ 5% NaCl solution saturated with H_2S at pH of 3.2, the threshold stress for no failure increased with the yield strength but turned to decrease when the yield strength exceeded a critical value σ_c, indicating the involvement of plastic deformation in the effects. Grain refinements shifted σ_c to higher values.

On the other hand, from microscopic viewpoints focusing on strain-induced lattice defects, grain-size effects on tensile properties were examined for martensitic steel in a fine-grain size range [19]. Plate specimens of 2 mm in thickness and 10 mm in width of 0.36C-0.97Si-0.20Mn-1.0Mo-0.2Cu (mass %) steel were repeatedly induction-heated and water-spray quenched to refine the prior austenite grain size in the range of 24–4.2 μm, followed by tempering at 823 K to the tensile strength of 1350 MPa. Three states of specimens, as-heat treated, plastically deformed to 5%, and subsequently annealed at 523 K for 1 h. Detection of lattice defects in specimens utilized hydrogen as the tracer, evaluating the tracer-hydrogen absorption capacity by TDA.

Figure 8.7 [19] shows the amounts of tracer-hydrogen in specimens of various grain sizes at the three states. The amounts in the as-heat-treated specimens substantially increased with the gran refinement below 10 μm. Plastic deformation remarkably increased the hydrogen absorption capacity, in accordance with previous results in Fig. 3.2 for iron, but the total amount of tracer-hydrogen decreased with grain refinement. Subsequent annealing at 523 K after straining eliminated almost the increment due to straining. The results are consistent with Fig. 3.4, implying that vacancy-type lattice defects are the trap sites of the incremental amounts of tracer-hydrogen associated with plastic deformation

Fig. 8.7 The amounts of tracer-hydrogen introduced to medium-carbon martensitic steels with various grain sizes. ○: As-heat treated, ●: Strained to 5%, Δ: Annealed at 250 °C (523 K) for 1 h after straining (Fuchigami et al. [19])
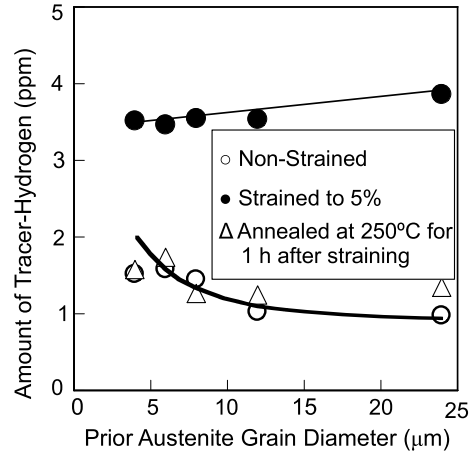

The lower solid line in Fig. 8.7 is the calculated curve of the total hydrogen concentration, C_{TOT}, which is the sum of the hydrogen concentrations in prior austenite grain boundaries C_{GB} and that in the matrix C_M, which includes hydrogen trapped in other lattice defects such as dislocations and martensite lath boundaries. The C_{GB} is the product of the total grain-boundary surface area and the hydrogen mass in the unit area of boundaries. C_{TOT} in the mass ratio is

$$C_{TOT} = C_{GB} + C_M$$
$$= 2a/\rho\overline{L} + C_M \tag{8.1}$$

where a is the hydrogen mass in unit area, ρ is the density of the steel, and $\overline{L}$ is the mean lineal intercept of grains obtained experimentally. The numerical values of a and C_M were determined from six combinations of observed C_{TOT} for four grain sizes shown in Fig. 8.7. The fit of the calculated curve with experiments implies that the increase in the hydrogen absorption capacity associated with grain refinement is simply due to the increase in grain-boundary surface area when the same hydrogen concentration in the unit area was assumed. The estimated values of a corresponded to the site coverage of 0.14 in grain-boundary areas when the monolayer plane was assumed for boundaries to have the same nearest inter-atomic distance as in bulk. The magnitude of a less than unity is reasonable, but actual values might be less when the thicknesses of boundaries are taken into account.

An important result of Fig. 8.7 is that the strain-induced increment of the hydrogen absorption capacity is reduced by grain refinement, i.e., the grain refinement suppresses the strain-induced creation of vacancies. Then, tensile tests were conducted with specimens with and without hydrogen precharging at the strain rate of 2.8×10^{-5} s^{-1}. Cathodic hydrogen precharging was given under a mild condition in a 3% NaCl aqueous solution containing 3 g/l NH$_4$SCN at a current density of 10A/m^2 for 18 h. Since simultaneous hydrogen charging was absent, the hydrogen

Fig. 8.8 Embrittlement index at tensile tests as a function of the increase in the amounts of tracer-hydrogen by straining to 5% (Fuchigami et al. [19])
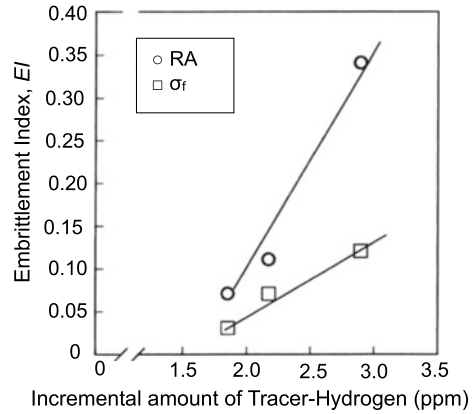
concentration in the unit area of grain boundaries was constant during the tensile test. Observed degradations of fracture stress and ductility were expressed in terms of the embrittlement indices, EI, defined as the fraction of the decrease in fracture stress σ_f or reduction of area RA in the form of

$$\mathrm{EI}_{\sigma_f} = \frac{\sigma_{fA} - \sigma_{fH}}{\sigma_{fA}}, \; \mathrm{EI}_{RA} = \frac{RA_A - RA_H}{RA_A}, \tag{8.2}$$

where subscripts H and A denote specimens with and without hydrogen precharging, respectively.

Figure 8.8 [19] shows the dependence of *EI* on the increment of the amount of tracer-hydrogen with straining to 5%. Together with the annealing effect shown in Fig. 8.7, the results of Fig. 8.8 imply that the effects of grain-size refinement on reducing the degradation are due to the decrease in the density of strain-induced vacancy-type defects. The generation of vacancies mostly results from mutual interactions of dislocations. Grain refinement may reduce the slip length and then the densities of dislocations in areas near grain boundaries that impede the slip extension. Correspondingly, the grain-size refinement should reduce hydrogen effects on fracture morphology. The hydrogen effect of changing the fracture mode from dimple to flatter QC was observed for specimens of 24 μm in grain size.

8.1.4   Impurities and Alloying Elements

(a)   Impurities

Intergranular fracture (IG) is typical in HE of severely embrittled high-strength steel, and impurities play a significant role in IG fracture. It has been well established that step cooling at tempering enhances temper embrittlement of martensitic steel, promoting segregation of impurity elements mostly of 14th and 15th groups such as

P, As, Sb, and Sn in the periodic table. Hydrogen accumulates along grain boundaries, as tritium autoradiography shows in Fig. 2.16, but the decrease in the Charpy impact fracture toughness that characterizes temper embrittlement does not appear in the case of hydrogen embrittlement (HE). The origins of IG fracture in temper embrittlement and HE are not certain to be identical. A cooperative relationship between temper embrittlement and HE has been the subject of extensive studies as reviewed by McMahon [20].

The enhanced susceptibility to HE by temper embrittlement was demonstrated in delayed fracture tests of HY 130 steel (0.1C-0.9Mn-0.35Si-5Ni-0.5Cr-0.5Mo-0.08 V in mass% and 900 MPa in the yield stress) in 0.1 N H_2SO_4 with As_2O_5, using edge-notched cantilever specimens [21] as described about IG fracture in Sect. 7.2.4. Step cooling drastically decreased the lowest applied stress intensity K_{TH}, i.e., the threshold to cause a fracture, from that of unembrittled specimens. K_{TH} normalized by the fracture toughness in the air was much lower for step-cooled specimens than unembrittled ones. Accordingly, a cooperative function of hydrogen and temper embrittlement was concluded.

Kameda and McMahon extensively examined the effects of impurities in fracture mechanics tests of 0.3C-3.5Ni-1.7Cr (mass %) steel doped with P, Sn, or Sb [22]. Grain-boundary concentrations C_{gb} of impurity elements were controlled by varying the aging time at 753 K on tempering and were estimated using Auger Electron Spectroscopy (AES). The threshold stress intensity K_{TH} for the first detectable crack extension at compact tension tests using pre-cracked specimens and the threshold stress σ_{th} for the microcrack formation at four-point bend tests using notched specimens were measured. K_{TH} and σ_{th} decreased with increasing C_{gb} of impurity elements in tests in air and 0.17 MPa hydrogen gas. In partially embrittled specimens, significant effects of hydrogen in reducing both K_{TH} and σ_{th} appeared, but hydrogen effects were smaller for lower K_{TH} and σ_{th} levels. The latter results are indicative of the involvement of some plasticity to induce HE.

Suppression of IG fracture is a prospective means to reduce the susceptibility to HE for high-strength steel, and reducing impurity segregation in prior austenite grain boundaries must be an effective method. Precipitation of proeutectoid ferrite along austenite grain boundaries was attempted according to this notion [23]. Proeutectoid ferrite of 3.5 ~ 8.4% in the areal fraction on the micrograph was precipitated in medium-carbon martensitic steel by isothermal holding at intermediate temperatures during quenching from the austenitizing temperature. Tensile strengths were fixed at almost the same level of about 1300 MPa by varying tempering temperatures between 623 and 693 K. Sustained-loading delayed fracture tests were conducted by immersing round bar specimens of 5 mm in diameter in 20% NH_4SCN aqueous solution at 323 K. Figure 8.9 [23] shows test results in which open marks denote steels without proeutectoid ferrite.

Proeutectoid ferrite markedly improved delayed fracture characteristics. The IG fracture near the crack initiation site for fully martensitic steel was absent by the precipitation of proeutectoid ferrite, and QC replaced IG. Proeutectoid ferrite

Fig. 8.9 Delayed fracture diagrams of high-strength martensitic steels. Solid and open marks denote steels with and without intergranular ferrite precipitation (Watanabe et al. [23])
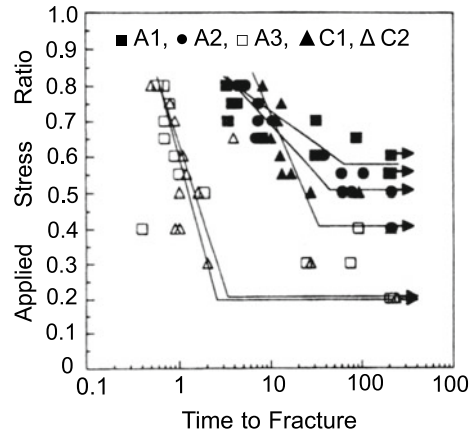
increased the hydrogen absorption capacity, but the amounts of hydrogen at the time of fracture were not systematically correlated with delayed fracture characteristics for different steels, even under the same applied stress. On the other hand, the mean hydrogen occlusion rates, defined as the hydrogen content in a failure specimen divided by the time to fracture, are shown in Fig. 8.10 [23] at the applied stress of 0.8 of the tensile strength. The time to fracture at a given applied stress was substantially scattered, but the no-failure threshold stresses shown in Fig. 8.9 correlated well with the mean hydrogen occlusion rates. The hydrogen content measures lattice defects that operate as hydrogen trap sites. Since most hydrogen in failure specimens is diffusive and vacancies are major trap sites of increased hydrogen contents by straining, the hydrogen occlusion rate likely represents the vacancy creation due to interactions between dislocations near grain boundaries. Proeutectoid ferrite likely reduces the local dislocation density near grain boundaries.

Fig. 8.10 Mean hydrogen occlusion rates per hour at sustained-loading delayed fracture tests at the applied stress of 0.8 of the tensile strength. Areal fractions of proeutectoid ferrite are 3.5, 8.4, and 0% for A1, A2, and A3 steels, respectively (Watanabe et al. [23])
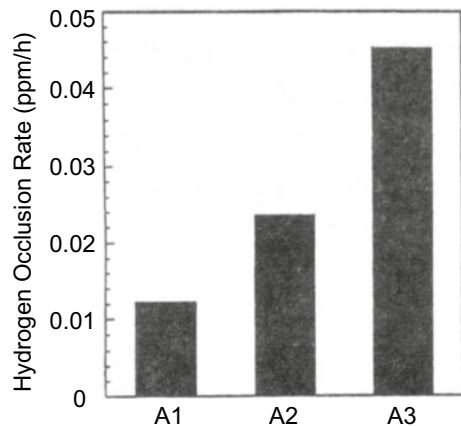
(b) Alloying elements

Impurity elements play the primary role in temper embrittlement of steel, but common alloying elements Mn and Si in steel also affect the susceptibility to HE [24]. Modified WOL tests for HY 130 steel in hydrogen gas of 0.21 MPa at room temperature exhibited a decrease in the threshold stress intensity K_{TH}, defined as the crack initiation on loading, by step cooling from tempering at 755 K. The degradation was much smaller for steel of very low Mn (0.02%) and Si (0.03%) contents than steel of standard compositions. Four-point bend tests in air and hydrogen gas were also conducted using notched specimens. A steel of standard compositions and step-cooled at 753 K for 1000 h exhibited a prominent decrease in fracture stress when tested in hydrogen gas than in air. Observations of the crack path revealed the crack initiation along plastic hinges or slip lines in the steel with reduced Mn and Si. In the steel of standard compositions, step cooling diminished the extent of the plastic region, and IG fracture mode prevailed.

Extensive studies on the effects of Mn and Si, as well as P and S, on the susceptibility to HE, were made by Bandyopadhyay et al., using modified WOL pre-cracked specimens of AISI 4340-type steel of various Mn and Si contents [25]. K_{th} values at the crack arrest in 0.11 MPa hydrogen gas exhibited a linear decrease against a parameter [Mn + 0.5Si + S + P (mass%)] up to 0.2. The decrease in K_{th} was associated with the increase in the area fraction of IG surface. Further, K_{th} values of commercial and high-purity steel in various hydrogen gas pressures were plotted uniquely on a single curve against a parameter $[10^4 C_H]$ + [Mn + 0.5Si + S + P in mass %]. Estimating the hydrogen concentration C_H was from Sieverts' law, and the accumulation in the stress field ahead of the pre-crack used Eq. (1.11). Bandyopadhyay et al. claimed that hydrogen and metalloid impurities additively operate in intergranular cohesion and that the function of Mn and Si is to control the segregation of P and S in austenite grain boundaries [25].

A cooperative function of P and Mn was observed for the threshold stress for no failure at SSC tests of martensitic steel [18]. The threshold stress decreased with increasing P contents, and the decrease at a constant P content was prominent with increased Mn contents. The yield strength was almost the same, ~745 MPa, but the fracture surface changed from transgranular to partially IG, associated with the decrease in the threshold stress.

The enhanced IG fracture by hydrogen at tensile tests of medium-carbon Cr–Mo martensitic steel plates with increasing Mn contents are shown in Figs. 7.6 and 7.7 in Sect. 7.2.4. The fracture mode was mainly IG, and the higher Mn contents caused smoother fracture surfaces and reduced accompanying fine tear patterns. Tensile test results under simultaneous hydrogen charging are shown in Fig. 8.11 [26]. The Mn contents did not affect tensile properties when hydrogen was not present, but the presence of hydrogen decreased the fracture stress and tensile ductility with increasing Mn contents. This result is consistent with other studies on K_{th} for AISI 4340 steel [22].

A crucial finding concerning Mn contents was that higher Mn contents pronounced increased hydrogen absorption capacity after straining, as shown in Fig. 7.20. TDA
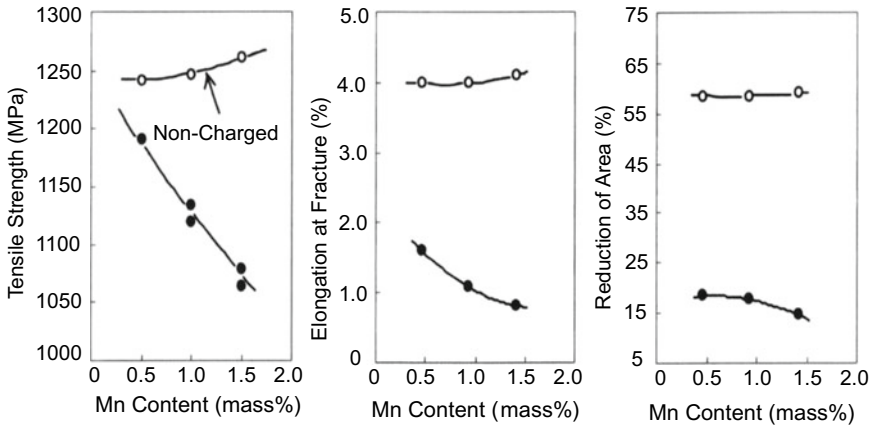
Fig. 8.11 Tensile properties of medium-carbon martensitic steels with different Mn contents with/without hydrogen charging (Nagumo et al. [26])

revealed the vacancy-type nature of the trap sites, as shown in Fig. 7.21. The increase in the density of strain-induced trap sites is apparently against the reduction of plasticity on the fracture surface. However, the results are plausible when extremely localized strain in regions close to prior austenite grain boundaries intensifies the accumulation of damage there, leading to premature fracture. A high dislocation density caused by the constraint of the slip extension across grain boundaries must favor the strain-induced creation of vacancies. The microstructural entity of Mn operating for strain localization is not definite quantitatively, but Mn likely affects structural factors such as impurity segregation and precipitation of carbides in grain boundaries, as suggested in preceding studies.

Boron is a unique element that intensifies the hardenability of steel with contents as low as ppm by segregating at the austenite grain boundary. Boron combines with nitrogen forming fine BN, and other alloying elements as well as thermal histories affect the states of B in steel. Effects of B on HE were examined at delayed fracture tests for 0.15%C-Si-Mn (mass%) martensitic steel containing different amounts of B and N [27]. A two-step austenitization was occasionally employed to fix B as fine BN precipitates in the matrix. Constant load delayed fracture tests were conducted, using cantilever bend-notched specimens under cathodic electrolysis in a 3% NaCl solution at current densities of 2 ~ 10 A/m^2. The fracture mode was mainly IG, and Auger electron spectroscopy (AES) on the IG fracture surface revealed separate peaks due to B and BN. Figure 8.12 [28] shows the threshold stress for delayed fracture as a function of B concentrations at grain boundaries calculated from AES peak heights. The B concentrations at grain boundaries were substantial, but segregated B was not harmful when its amount was limited. On the other hand, fine precipitates of BN at grain boundaries remarkably decreased the threshold stress. Fixing N as TiN by Ti addition and precipitation of BN in the matrix by two-step austenitization are useful means to suppress detrimental effects associated with B addition.

Fig. 8.12 Threshold stress for no failure at delayed fracture for B-containing martensitic steels as a function of B concentrations at prior austenite grain boundaries. Segregation Boron and BN precipitates are separated by Auger electron spectroscopy (Inoue et al. [28])
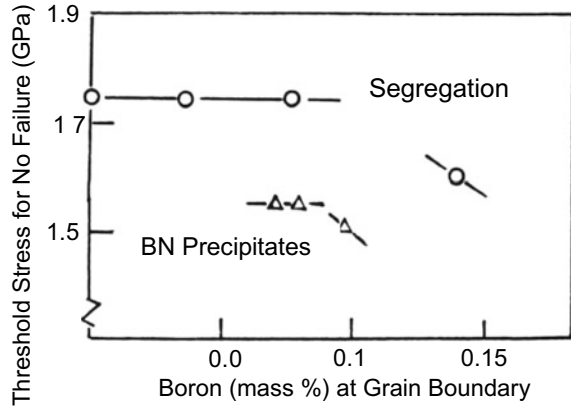
8.1.5 Microscopic Features of Fracture

Fractographic features of martensitic and bainitic steel in HE are mainly IG or QC. Kim and Morris noticed {110} or {112} fracture plane after hydrogen embrittlement, while {100} cleavage plane is predominant in low-temperature fracture [29]. The steel was 0.06C-5.86Ni-l.21Mn-0.69Cr-0.2Mo-0.2Si (wt. %) in compositions and 1073 and 873 K of austenitizing and tempering temperatures, respectively. After hydrogen charging by cathodic electrolysis in 1 N H_2SO_4 + small amounts of As_2O_3 and CS_2 at 160A/m^2, which gives a pretty high hydrogen fugacity, a three-point bending test was applied. Hydrogen charging reduced the fracture toughness from 330 MPa·$m^{1/2}$ to 180 MPa·$m^{1/2}$.

Scanning electron microscopy (SEM) of the fracture surface exhibited fine, lath-like features comparable in dimension to the martensite laths, as described in Sect. 7.2.3 [29]. Chemical etching of the fracture surface showed etch pits of the elongated-hexagon shape, typical of etch pits on {110} surfaces. Transmission electron microscopy (TEM) of the immediate subsurface region revealed that the fracture surface lies in the lath boundaries over almost its whole length. Further, high-resolution TEM fractography revealed a dense population of fine secondary cracks immediately beneath the fracture surface. The microcracks were found in the first few μm beneath the fracture surface, certainly formed ahead of the propagating crack tip.

Shibata et al. precisely observed subsurface microcracks in 0.1%C lath-martensitic steel austenitized at 1323 K and iced-brine quenched [30]. Tensile curves of specimens were similar between specimens with and without hydrogen charging, but fracture of the hydrogen-charged specimen occurred soon after the elastic limit. Almost all areas of the fracture surface consisted of fine and shallow dimple patterns, and microcracks in an area about 200 μm beneath the fracture surface were almost perpendicular to the tensile axis. All observed microcracks were located on or close to the prior austenite grain boundary.

Fig. 8.13 SEM image of the fracture surface of the hydrogen-charged Fe-0.4C steel tempered at 623 K. The white arrows indicate surfaces with striations (Shibata et al. [31])
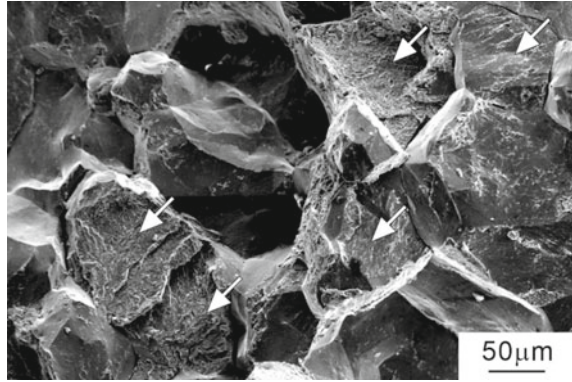

Shibata et al. compared the fracture surface and the cross-section of as-quenched 0.1% C and tempered 0.4% C martensitic steels [31]. The 0.4% C steel was austenitized at 1123 K and tempered at 573, 623, and 723 K after ice-brine quenching. In the 0.4% C steel, film-like carbides precipitated on martensite lath boundaries, and the dislocation density inside the lath decreased with increasing tempering temperatures. Cathodic hydrogen charging was in 1 N H_2SO_4 + 2 mg/l As_2O_3 at a current density of 100 A/m^2.

On a slow strain-rate tensile test, the hydrogen-charged 0.4% C steel tempered at 573 K and 623 K fractured within the apparently elastic range [31]. As shown in Fig. 8.13 [31], the fracture surface was faceted intergranular (IG)-like, but most of the fracture surfaces exhibited striations, such as tear ledge patterns indicated by arrows. On the cross-section, SEM images revealed several microcracks located along or close to the prior austenite grain boundaries, but they were parallel to {011} planes within the prior austenite grain. Electron backscattering diffraction (EBSD) analysis of the crystallographic orientation demonstrated that the facet components on the fracture surfaces were parallel to {011} planes.

The involvement of plasticity in forming fracture surfaces is common for IG, QC, and fine dimples in HE. The preference of each morphology in fracture was investigated by Shibata et al. [32] using fracture surface topography analysis (FRASTA) [33]. The used steel was a 0.1C-8Ni steel sheet of 1.7 mm thickness, austenitized at 1373 K, followed by ice-brine quenching. After hydrogen charging by cathodic electrolysis in 3% NaCl + 3 g/l NH_4SCN at a current density of 5 A/m^2, a slow strain-rate tensile test at 8.3×10^{-6}/s was conducted. FRASTA is a computational reconstruction of the fracture process by comparing topographic features of mating fracture areas [31]. Its application revealed the sequence of fracture morphology change of smooth surface → surface with serrated markings → dimple surface. Figure 8.14 [32] shows the evolution of each fractographic feature on separating the initially matched fracture surfaces. Evidently, the smooth surfaces along prior austenite grain boundaries are the first (weakest) sites to separate.

The hydrogen-related fracture of martensitic steel is different from conventional brittle cleavage fracture of iron and steel, and the involvement of local plasticity is

Fig. 8.14 Change in fraction of fracture modes in FRASTA as a function of separation distance between the two topographic maps (Shibata et al. [32])
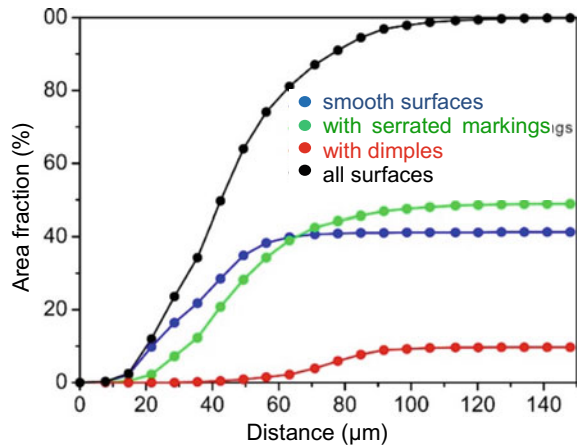
definite. The lath structure constrains the operative slip system. Dislocation activities in as-quenched 0.13% C lath-martensitic steel were analyzed by Miyauchi et al. using the EBSD pattern technique [34]. The rotation of each martensite block was investigated and compared with that predicted by the Taylor and Sachs models. Slip systems of slip planes parallel to the lath and block boundaries, i.e., {011} planes, were preferentially activated. From 0 to 8% tensile strain, lath-constrained crystal rotation was confirmed for about three-quarters of all martensite blocks studied. In the early deformation stage, almost only slip systems in the lath-plane operate, and long-distance dislocation slip is not feasible.

8.2 Multiphase Steel

Recent industrial developments require materials to fit energy saving, as typical in weight-reducing automobiles. High-strength low-alloy steel has been well developed, but recent advanced high-strength steels (AHSSs) mostly utilize multiphase techniques such as Dual Phase (DP), Transformation Induced Plasticity (TRIP), Twinning-Induced Plasticity (TWIP), Complex Phase (CP), and Ferritic Bainitic (FB) steel. The enhanced susceptibility to environmental degradation is a crucial problem associated with high strengthening. Various factors operate in HE, and comprehensive studies about each type of steel are now in progress [35, 36]. Accordingly, in the present stage, limited descriptions, rather than comprehensive, focus on elementary findings likely common in the fracture process.

8.2.1 Dual Phase Steel

The dual phase (DP) steel of microstructures consisting of finely dispersed martensite in ferrite matrix is a prospective type of high-strength steel because of its good combination of strength and workability. In an early work, Davies prepared dual phase structures of ~ 0.1% C steel either by air cooling from the intercritical ($\alpha + \gamma$) region or water quenching from an intercritical temperature and tempering at about 433 K for a few minutes [37]. Hydrogen-charging conditions using cathodic electrolysis in 4% H_2SO_4 were determined to produce no permanent damage to the structure. Tensile test results showed a substantial decrease in uniform elongation by hydrogen, but the reduction totally recovered in specimens tempered at 773 K. The fracture surface of the hydrogen-charged specimens showed large dimple-like facets of ~ 5 μm in size but containing river-like striations.

Details of microstructures and the crack path were not presented, but Davies showed that the presence of martensite evolved HE of the DP steel. DP steels did not contain boundaries between prior austenite grains but only ferrite-ferrite boundaries and ferrite-martensite interfaces. The no-failure critical stress for delayed fracture decreased by the presence of martensite, but it was above the macroscopic yield stress. It was then concluded that high-carbon martensite is responsible for HE of dual phase steel, but considerable macroscopic deformation is involved in the failure.

Davies further prepared DP steel of (0.03–0.12)C-0.2Si-0.5Mn-0.5Mo (mass%) in compositions containing martensite of 5–45% in volume fraction [38]. The tensile strength of the steel increased from about 400–900 MPa with increasing martensite volume fractions, accompanying a decrease in ferrite grain size and an increase in martensite size. The susceptibility to HE was evaluated by tensile tests using specimens hydrogen charged in poisoned 4% H_2SO_4 at a current density of 60A/m^2.

As a function of martensite volume fraction, the reduction in the uniform elongation of specimens as the ratio between with and without hydrogen charging showed three ranges, as shown in Fig. 8.15: (1) no embrittlement up to 10% martensite, (2) advancing embrittlement from 10 to 30%, and (3) essentially independent of martensite contents above 30%. All regions of martensite were at ferrite grain boundaries. The regions were separated in the steel containing martensite less than 10% but tended to form a network over the range of 10 to about 30%, associated with decreasing ferrite grain size and increasing martensite region size.

Martensite likely acts as the easy path for crack propagation. Effects of martensite volume fraction differed by compositions of steel. As included in Fig. 8.15, a commercial DP steel of 0.1C-1.5Mn-0.55Si-0.08 V (mass %) in compositions with fine ferrite grain size of 3–5 μm showed a constant and higher hydrogen degradation than other steels. In the commercial steel, the increase in martensite volume fraction from 20 to 40% raised the tensile strength from 800 to 1100 MPa, but the ferrite grain size was much finer. The estimated carbon content in the martensite for the experiments was more than 0.2%.

Koyama et al. prepared a 0.15% C ferrite/martensite DP steel by water quenching from the two-phase region [39]. Tensile test results showed a substantial decrease

Fig. 8.15 Ratios of uniform elongations at tensile tests with/without hydrogen charging for ferrite-martensite dual phase steels. Alloys 1–5 contain about 0.5% Mn and 0.5% Mo, Alloy 6 contains 1.46% Mn and 0.08%V without Mo. Alloy #6 (●) is a commercial dual phase steel (Davies [38])
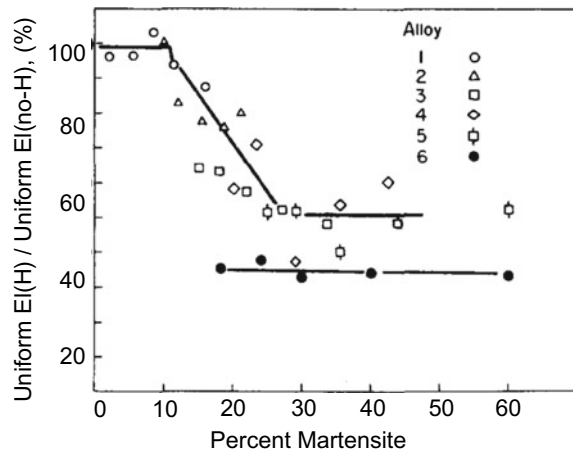
in the total elongation by hydrogen charging, and the fracture surface consisted of fine dimples and large brittle feature regions. Hydrogen charging increased the size of the brittle feature region, which contained a considerable number of voids and dimples. In the early stage of failure, in situ SEM observations detected cracking of martensite in both hydrogen-charged and uncharged specimens. Hydrogen effects were apparent in the late stages of deformation. When hydrogen was not present, crack propagation inside the ferrite grains was not observed, consistent with earlier studies [37, 38]. In hydrogen-charged specimens, the crack propagated along the prior austenite grain boundaries through a few neighboring ferrite grains, associated with increased local orientation changes around the crack tip. The findings suggest a cooperative function of martensite and ferrite in hydrogen-related changes of deformation microstructures. Fracture surfaces showed both dimple and brittle features. Hydrogen charging increased the size of brittle feature regions, but sizable brittle feature regions contained many voids and dimples.

Koyama et al. also examined microscopic features of fracture in DP steel [39]. Hydrogen promoted the necking onset and the evolution of the damaged area during straining. The term "damage" used by Koyama et al. indicates flaws such as cracks and voids. An image quality (IQ) map in EBSD, that represents the crystallinity of the diffracting area, revealed an incipient crack nucleation in the incubation period, primarily within martensite before a substantial crack growth started, as shown in Fig. 8.16(a), (b) together with the rolling direction inverse pole figure (RD IPF) and Kernel average misorientation (KAM) maps in Fig. 8.16c, d [39].

On the other hand, KAM-distribution measures the orientation difference between neighboring areas. KAM map of undeformed specimens revealed that martensite contains a considerable amount of lattice defects. KAM maps were almost unaffected by the presence of hydrogen on straining up to 7% in both ferrite and martensite phases. The incipient cracks in Fig. 8.16 grew into neighboring ferrite grains in hydrogen-charged specimens. Changes in the local orientation and high KAM values around the crack tip in hydrogen-charged specimens suggested reduced

Fig. 8.16 **(a)** IQ map at a 1–2% local plastic strain (end of the damage incubation regime). The red arrows indicate cracks. **(b)** IQ, **(c)** RD IPF, and **(d)** KAM maps corresponding to the part surrounded by the square in (**a**) (Koyama et al. [39])
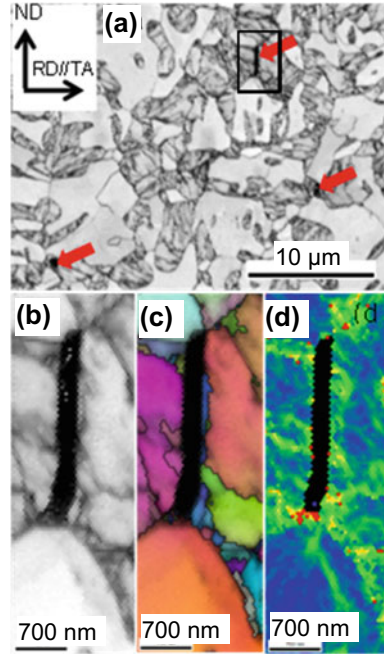
crack-arresting ability by hydrogen-affected plasticity. Koyama et al. proposed that hydrogen significantly affects the following crack propagation in martensite into the surrounding ferrite grains.

Furthermore, when the strain reached 7%, ferrite/martensite interface and martensite interior such as block boundary were also cracked [39]. The hydrogen-assisted cracking at multiple boundaries and crack propagation into ferrite promoted crack coalescence, which resulted in the distinct hydrogen-induced mechanical degradation of DP steel.

A comparison of delayed fracture characteristics between tempered-martensite and ferrite/tempered-martensite DP structures of the same tensile strength was conducted by Takahashi et al. for a 0.13C-1.4Si-2.2Mn (mass %) steel [40]. The tempered martensitic steel was prepared by austenitizing at 1153 K, followed by water quenching and tempering at 673 K, while the DP steel was prepared by austenitizing at 1093 K, followed by air cooling to 953 K, water quenching, and tempering at 423 K. The volume fraction of the martensite phase was about 60%. The tensile strength of the single martensitic and DP steel was similar, 1256 and 1217 MPa, respectively, while the yield stress was 1146 and 711 MPa, respectively. The specimens were given pre-loading at 1100 MPa in the air for 1 h just before the sustained-loading test. The applied stress of 1100 MPa at pre-loading was higher than the yield stress of the DP steel, and the pre-loading must have caused work hardening of ferrite, suppressing plasticity that generates damage.

In sustained loading, cathodic hydrogen charging in a 3% NaCl + 0.3% NH_4SCN aqueous solution at a current density of 5 or 50 A/m² started after applying the sustained loading. Since the specimen size was 6 mm in diameter, the hydrogen distribution in the specimen was not uniform in an early stage of sustained loading, limited by hydrogen diffusion. The time to fracture in the middle range of the applied stress, near the yield stress, was similar between the two structures. However, the critical stress for no failure of the dual phase steel (~400 MPa) was higher than that (~300 MPa) of the single-phase steel. A superior resistance to delayed fracture of 1500 MPa-class bainite/martensite DP high-strength steel, compared to single-phase martensitic steel, was shown by Gu et al. in terms of K_{ISCC} and crack growth rate [41]. The study used modified wedge opening loading (WOL) specimens in a 3.5% NaCl solution at 298 K.

8.2.2 Retained Austenite—TRIP Steel

In martensitic or lower bainitic steel, some fractions of retained austenite γ_R often exist in the form of thin films along lath boundaries. The hydrogen absorption capacity of the steel increases with the amount of γ_R, presumably due to the high solubility of hydrogen in austenite and to hydrogen trapping at the γ_R/matrix interface [42].

(a) Basic characteristics

Chan et al. prepared martensitic steels of different carbon contents and measured the effects of γ_R on the hydrogen content and the effective hydrogen diffusivity [42]. X-ray diffraction analysis detected γ_R in steel of carbon contents of more than 0.6%. In high-carbon steel, no appreciable difference in the amount of γ_R was detected before and after hydrogen charging. Microstructures of lightly deformed TRIP steel were characterized by Petrov et al. [43]. Electrochemical permeation experiments revealed that increasing carbon content increased γ_R and hydrogen contents while hydrogen diffusivity decreased. Table 8.1 [42] summarizes the results. Chan et al. deduced that the retained austenite itself does not trap hydrogen significantly, but the interfaces between γ_R and martensitic plates may be the possible trapping sites.

Retained austenite partially decomposes when stress is applied. Transformation-induced plasticity is utilized as TRIP steel to have high formability and fracture

Table 8.1 Effects of carbon content on the amount of retained austenite, effective hydrogen diffusivity, and hydrogen content in martensitic steel (Chan et al. [42])

Carbon content (wt %)	γ_R (Volume %)	D_{eff} (cm²/sec)	C_H (wt ppm)
0.23	–	4×10^{-7}	–
0.44	–	2×10^{-7}	–
0.64	3.1	1.4×10^{-7}	0.5
0.79	5.9	8×10^{-8}	1.1
0.93	9.8	6×10^{-8}	1.8

toughness while retaining excellent strength. Kim et al. investigated the $\gamma \rightarrow$ martensite phase transformation in the TRIP steel using in situ observation of the change in hydrogen permeation current under loading conditions [44]. A hot-rolled 0.07C-5Mn-0.5Si-2Al (mass %) steel sheet was cold-rolled and reheated at 1013 K for 2 min, followed by air cooling at 10 K/sec. The steady-state permeation current (i_{ss}) for the TRIP steel is much lower than that for the ferritic steel. Application of external load exceeding the elastic limit instantly decreased the permeation current due to the trapping of hydrogen atoms by newly generated dislocations. However, the current increased, going up much higher than the i_{ss} in the specimen with no additional loading. Kim et al. deduced that the cause is the hydrogen transport by newly generated dislocations and deformation-induced martensitic decomposition [44].

Hydrogen trapping in TRIP steel was investigated by Escobar et al. for 0.17C-0.4Si-1.6Mn-0.5 ~ 2Al steel sheets given cold-work of 3%, 10%, and 15% elongation [45]. Thermal desorption analysis (TDA) of hydrogen, introduced as a tracer, exhibited a large peak at about 90 ℃ (363 K) and a small peak at about 500 ℃ (773 K), as shown in Fig. 8.17 [45]. The main peak was asymmetric and consisted of two peaks. Increasing the degree of cold deformation, i.e., the amount of TRIP, substantially increased the lower-temperature peak and reduced the higher-temperature peak as shown in the inset of Fig. 8.17, consistent with Fig. 3.11 for deformed iron, while the higher-temperature peak at 773 K is from γ_R. Indeed, the lower-temperature peak in Fig. 8.17 is the desorption of hydrogen in solid-solution and trapped at dislocations and vacancies. The hydrogen binding energy of γ_R obtained by varying the heating rate at TDA was 90 ± 25 kJ/mol.

(b)   Susceptibility to hydrogen embrittlement

TRIP is a useful tool to improve the formability and fracture toughness of high-strength steel, but its susceptibility to environmental degradation is a crucial issue.
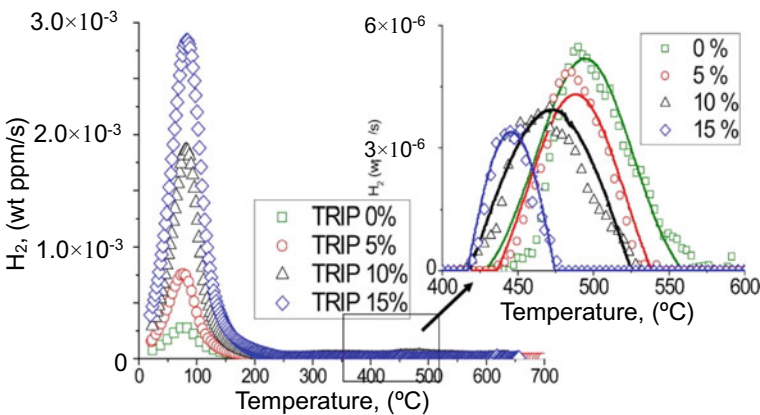

Fig. 8.17 Effects of cold deformation on the TDA spectrum of the TRIP steel. Heating rate 6.66 K min^{-1} (Escobar et al. [45])

Depover et al. compared hydrogen degradation of low-carbon TRIP, DP, Ferrite-Bainitic (FB), and high-strength low-alloy (HSLA) steel sheets in tensile tests using notched specimens [35]. Details of the sample preparation were not definite, but the tensile strength was 500 ~ 700 MPa levels. The amount of γ_R in the TRIP steel was 9.6%. Cathodic hydrogen precharging was in a 0.5 M H_2SO_4 + 1 g/l of thiourea solution for 2 h at 26.5 A/m^2. An embrittlement index (EI) was defined as the ratio of the decrement due to hydrogen in elongation or reduction of area to that of in the air. The test results showed that TRIP steel was most prone to hydrogen embrittlement (EI of 66%), followed by DP, FB, and finally the HSLA grade (EI of 32%).

On the other hand, the effects of carbon-partitioning in quenched medium-carbon (Q&P) steel [46] on hydrogen embrittlement were compared with a traditional quenching and tempering (Q&T) steel of identical chemical composition by Yang et al. [47]. Diffusion of carbon from martensite to γ_R was a means to stabilize γ_R against further transformation at lower temperatures. Yang et al. prepared Q&P steel by austenitizing 0.4C-1.5Mn-1.5Si (wt%) steel sheets at 860 °C (1133 K) or 950 °C (1223 K) for 5 min and then immersed some of them in a molten salt bath at a temperature of 513 K (T_q) for 15 s. Immediately transferring into another molten salt bath at 693 K (T_p) for 30 s, final water quenching was given. On the other hand, Q&T specimens were water quenched directly from 1133 K or 1223 K after 5 min holding and then tempered at 693 K for 120 s to prepare nearly the same tensile strength level with Q&P steel. The tensile strengths of the steels were over 1500 MPa.

The microstructures of all specimens were lath martensite, but EBSD and TEM observations revealed different amounts and morphologies of γ_R. The volume fraction and morphology of γ_R in Q&P 950 were about 17% and primarily blocky along martensite boundaries, while negligible volume amount in Q&T 950 specimens. In Q&P 860 specimens, γ_R was flake-like and about 18% in the volume fraction, while in Q&T 660 specimens, γ_R was film-like and much less volume fraction.

The susceptibility to HE was evaluated in slow strain-rate tensile (SSRT) tests using hydrogen-precharged specimens. Hydrogen precharging was by cathodic electrolysis in 0.2 mol/l NaOH with 2 g/l thioureas at a current density of 100 A/m^2. Earlier fractures in tensile tests occurred with longer hydrogen-charging time. The embrittlement index (EI) was defined as the decrement ratio due to hydrogen in elongation or reduction of area to that of in the air. Hydrogen embrittlement was substantial in all steels, but Q&P specimens showed a notably high HE resistance compared to the Q&T. Q&P 860 was the best, although EI was as much as 75% after 60-min hydrogen precharging.

On the contrary, a detrimental effect of blocky γ_R was reported [48]. Kobayashi et al. prepared bainitic ferrite microstructures of different volume fractions in low-alloyed 0.4% C steel by austempering (isothermal transformation above M_s temperature) at 698 K in a salt bath for various periods up to 10^4 min after austenitizing at 1223 K [48]. The tensile strength was about 1100 MPa. The amount of γ_R was about volume 20%, not systematically dependent on the holding time at austempering, and the carbon concentration in γ_R was about 1.2 ~ 1.5 mass %. The morphology of γ_R inside the martensite-austenite constituent was blocky and film-like at bainitic ferrite boundaries. Slow strain-rate tensile tests with and without hydrogen charging

exhibited substantial hydrogen degradation in the total elongation, much higher in the presence of blocky γ_R. γ_R partially decomposed into ferrite and carbides by applying plastic strain, but the effects of hydrogen and morphology on the stability were not so much significant.

The effects of γ_R on hydrogen embrittlement are complicated, depending on its volume fraction, distribution, morphology, and stability. Fresh martensite, as a product of the decomposition of γ_R, is not the definite cause of the degradation.

8.3 Austenitic Stainless Steel

Austenitic (γ-) stainless steel is one of the main types of steel with high corrosion- and heat-resistances. As described in Sect. 1.1 on solubility and in Sect. 4.1.1 on diffusivity, the basic behaviors of hydrogen in γ-steel are substantially different from those in ferritic steel. Coupled compositional and crystal-structural effects give some specific situations for HE of high alloyed austenitic steel. Attention to be paid is that the hydrogen distribution is often very inhomogeneous in γ-stainless steel due to the very low diffusivity of hydrogen at room temperature. On cathodic hydrogen charging to Type 310 stainless steel (21Ni-23Cr-2Mn-1Si in mass %) in 1 N H_2SO_4 with arsenic at a current density of 1000A/m^2, the estimated hydrogen concentration in the near-surface layers amounted to as high as 0.5 ~ 0.8 in H/M atomic ratio [49].

8.3.1 Hydrides and Phase Changes

Three types of hydrides have been reported on hydrogen charging to Ni-containing γ-stainless steel; β- and β'-phases of face-centered cubic (fcc) structures and the η-phase of a hexagonal close-packed (hcp) structure [50]. The η-phase is also denoted as ε' since η has a lattice constant some percent larger than that of ε-martensite. Hydrides form when hydrogen concentration is high enough. Figure 8.18 [51] shows X-ray diffraction patterns of Type 304 steel specimens of 0.8 mm in thickness and strongly cathodic hydrogen charged in poisoned 1 N H_2SO_4 at current densities of 100 ~ 1000A/m^2 at 293 K. At an early charging stage, ε' and an fcc Y-phase appeared. With increasing the charging time, Y-phase disappeared and ε' decomposed into body-centered tetragonal α'-martensite and ε phases.

The lattice constant of ε' is almost constant, implying that ε' is a hydride, whereas that of ε was larger than that of ε formed on cooling or straining. Hydrogen charging at 333 K (60 °C) induced two fcc phases instead of Y, likely corresponding to β and β'. The phase separation into ε' and fcc γ'-phase from γ was also reported for Type 310S steel when hydrogen concentration was 18 and 25 at.% at 308 K (35 °C) and 348 K (75 °C), respectively [51]. The Y-phase reported by Kamachi [51] may correspond to the γ'-phase reported by Ulmer and Altstetter [52].
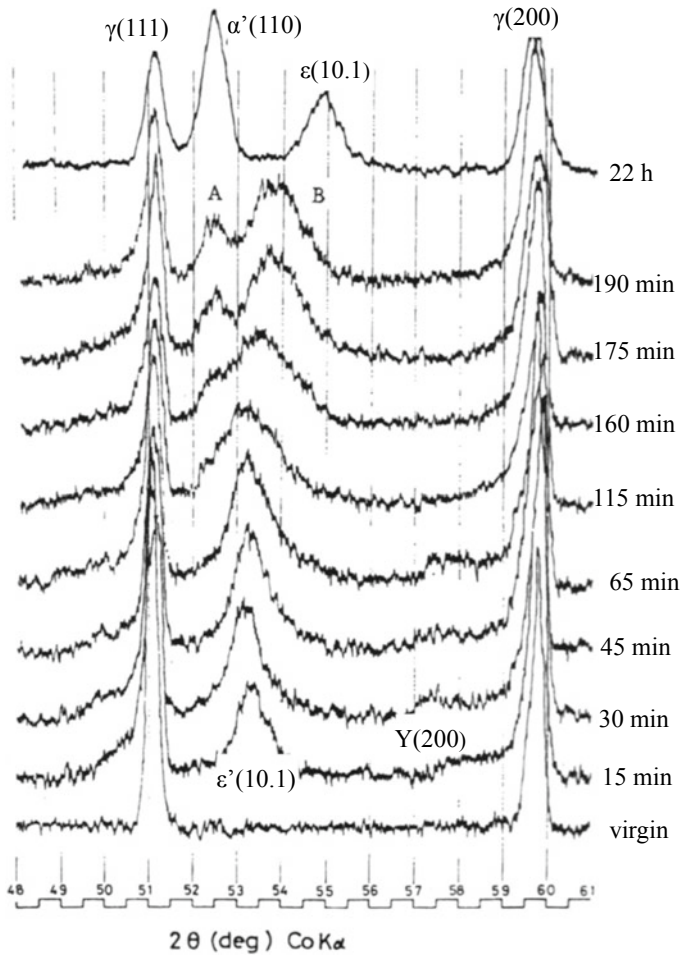
Fig. 8.18 Change in X-Ray diffraction patterns with the progress of hydrogen charging at 20 °C into Type 304 γ-stainless steel sheet (Kamachi [51])

The presence of α', susceptible to HE, is an issue as the origin of HE of unstable γ-stainless steels as described in the following Sect. 8.3.2. Crack path associated with α' is often observed in failure specimens. In this respect, an important finding is the reversible phase change of ε' to α' and ε during aging at room temperature, as shown in Fig. 8.19 [51]. Simultaneously conducted transmission electron microscopy observations revealed the formation of band-like α' within ε [51]. A similar formation of α' together with γ' and ε' was reported by Narita et al. during aging hydrogen-charged Type 304 [53]. The formed α' disappeared when hydrogen was recharged, indicating that α' and ε are reversible. An observed crack path after the crack extension was through or along α', but the actual crack extension might be
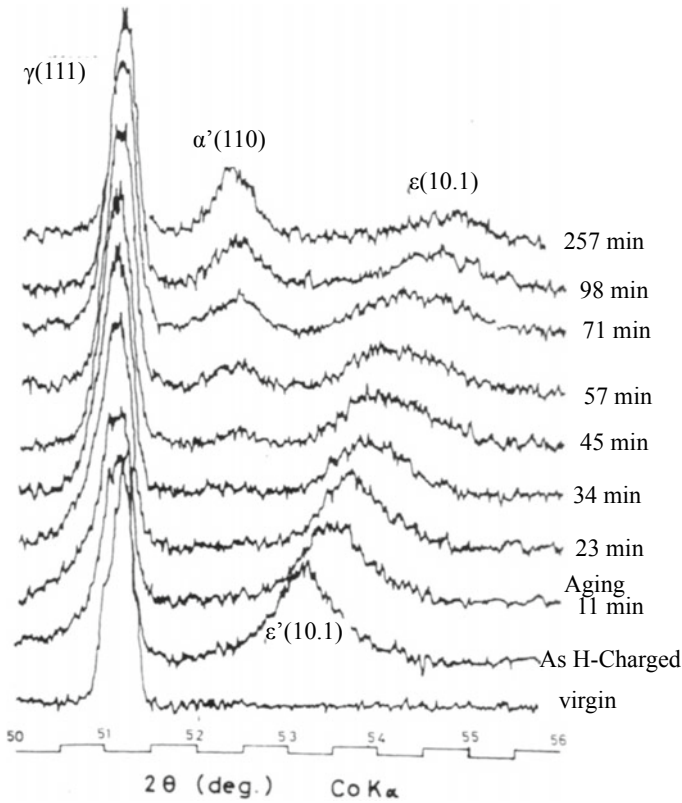
Fig. 8.19 Change in X-ray diffraction patterns from hydrogen-charged Type 304 γ-stainless steel during aging at room temperature (Kamachi [51])

through or along ε. For Type 310S, the formation of α' was not observed at hydrogen charging and outgassing.

Two different hydrogen functions have been proposed as the driving force of hydrogen-induced phase changes. The one is the stress-induced effect due to a significant lattice expansion that interstitial hydrogen causes. As a support, stress-induced cracking associated with hydrogen degassing appeared as fine surface cracks by shrinkage in hydrogen-charged Types 304 and 310S steels [53]. Very high concentrations of hydrogen favor to occur such situations. In this case, the stress-induced phase change is not likely in Type 310S because the deformation-induced martensite start temperature, M_d, is well below room temperature.

Alternatively, Iyer discussed some intrinsic effects of hydrogen on the thermodynamic stability of γ-phase [54]. In analogy to other interstitial solute atoms such as carbon and nitrogen, hydrogen was assumed to stabilize the γ-phase, retarding the transformation to martensite. Some observations, such as a more considerable

amount of retained austenite associated with higher hydrogen content, support the notion.

However, no effects of hydrogen were observed for the martensite start temperature, M_s, of Fe-30Ni alloy for hydrogen up to 400 at. ppm, i.e., no effect in stabilizing austenite [55]. Also, hydrogen did not affect volume fractions of deformation-induced α' and ε in Type 304L and α' in Types 301 and 310S [55]. Narita et al. postulated that hydrogen stabilizes ε [53]. Since hcp ε-phase may form as the result of the motion of partial dislocations leaving arrays of stacking faults, increases in M_S and M_d are feasible if hydrogen lowers the stacking fault energy. However, reported hydrogen effects are not always consistent. Hydrogen effects on γ-steel depend on experimental conditions such as hydrogen concentration, temperature, and specimen thickness. Careful examinations are necessary for employed experimental procedures.

## *8.3.2   Compositional Effects on Hydrogen Embrittlement*

The susceptibilities to HE of γ-stainless steel vary by the type of steel. Figure 8.20 shows tensile test results of Types 304 and 310 steel sheets, hydrogen precharged to about 12 mass ppm and continuing charging during tensile tests [56]. Unnotched smooth specimens of 0.1 mm in thickness were cathodic hydrogen charged in poisoned 0.5 N H_2SO_4 at current densities ranging from 0 to 300A/m^2. The yield stress was not affected by hydrogen, whereas the elongation to fracture and the area under the tensile stress–strain curve decreased with increasing current densities. The degradation appeared in each steel but more pronouncedly for Type 304 steel.

(a)   Stability of austenite

The stability of γ-stainless steel against martensite transformation is crucial for HE. Effects of test temperatures and nickel contents on hydrogen degradation are shown in Fig. 8.21 [57] for three types of steel containing 18% Cr and different nickel contents. The contours in Fig. 8.20 show equal fracture strain in percent, and the filled marks and the region under the dotted line indicate the presence of α' martensite after the test. The region of significant degradation overlaps, though not exactly, that of α' formation.

The specification of a steel type admits certain compositional ranges. Table 8.2 shows the chemical compositions of two Type 304 steel. Steel B is slightly more stable than Steel A against the deformation-induced α'-transformation according to magnetic measurements [58]. Susceptibilities to HE differed between the two steels of the same type. Hydrogen effects on the threshold stress intensity K_{TH} for the crack initiation and the crack growth rate were measured using single-edge-notched specimens under constant load at room temperature. Hydrogen up to 50 mass ppm was uniformly precharged by cathodic electrolysis in a molten salt bath at 553 K. The K_{TH} decreased with increasing hydrogen contents, but K_{TH} was higher, and the Stage II crack growth rate was lower for Steel B than Steel A at the same hydrogen

Fig. 8.20 Tensile properties
of Type 304 and Type 310
steels under hydrogen
charging at various current
densities (Inoue et al. [56])
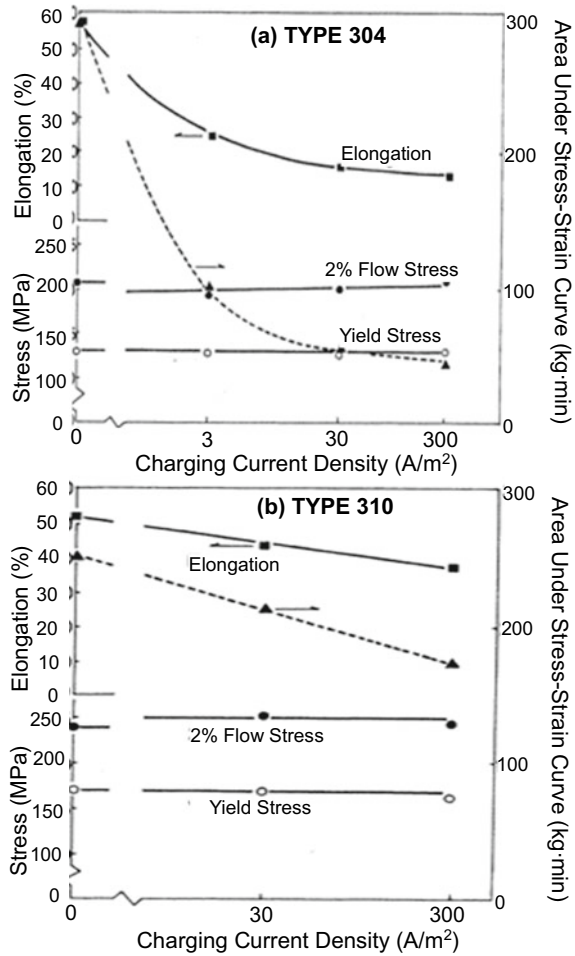
contents. However, the amounts of deformation-induced α' were not affected by
hydrogen for these steels. It may suggest that the stability of the γ-phase is crucial
to HE, but the effect not necessarily results from the formed α'-martensite.

(b) Sensitization

Sensitization, i.e., isothermal heat treatments in the temperature range between 773
and 1123 K, enhances intergranular corrosion and stress corrosion cracking of γ-
stainless steel. The reason is the precipitation of chromium carbides at grain bound-
aries, resulting in the depletion of Cr and C around the precipitates. Enhanced suscep-
tibilities to HE by sensitization were reported for Type 304 steel [58]. On delayed frac-
ture tests using smooth bar specimens under cathodic hydrogen charging, the lowest
applied stress to cause delayed fracture decreased by the sensitization associated
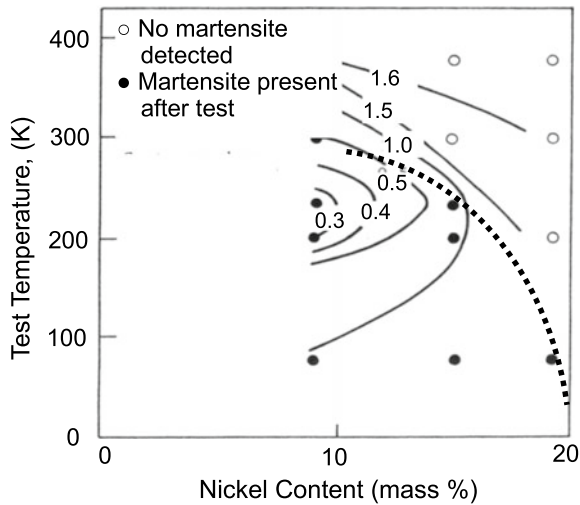with IG fracture morphology.

Fig. 8.21 Isoductility diagram for hydrogen-charged Fe–Cr-Ni alloys. Contours show equal values of plastic strain (Caskey [57])

Table 8.2 Chemical compositions of two Type 304 stainless steel (in mass %) (Singh et al. [58])

Alloy	C	N	Cr	Ni	Mn	Si	Mo	Cu
A	0.061	0.041	18.0	8.54	1.72	0.58	0.18	0.28
B	0.061	0.027	18.2	9.42	1.33	0.59	0.14	0.26

Susceptibilities to HE on tensile tests of various γ-stainless steel at low temperatures in 1 MPa hydrogen and He gases are shown in Fig. 8.22 [59] in terms of the ratio of the reduction of area in the two environments. Notations (S) and (SD) in Fig. 8.22, respectively, indicate "sensitized" and "desensitized" by annealing at 1193 K for 8 h. The maximum degradation by hydrogen occurred at the test temperature of around 220 K, and the degradation in Type 304 was more prominent than Type 316. However, the effects of sensitization on further degradations and its recovery by desensitization were significant in Type 316, while almost immune in Type 304. Fracture morphologies IG in sensitized and QC in desensitized specimens were common in the two steel types. Transmission electron microscopy revealed $Cr_{23}C_6$ and α' along grain boundaries in sensitized Type 304. In desensitized specimens, discontinuous carbides along grain boundaries still existed, but no α' was identified. The case of Type 304 implies that α' itself is not the cause of degradation, and the low stability of γ in Type 304 might be influential in degradation. Fractographic features of sensitized and desensitized specimens are described in the following Sect. 8.3.3.

In Fig. 8.22, stable Type 310S did not exhibit HE. Type 309S (0.06C-14Ni-23Cr in mass %) was also stable without degrading at tensile tests in 69 MPa hydrogen gas at room temperature [60]. However, increasing the hydrogen concentration by

Fig. 8.22 Temperature dependencies of the susceptibility to hydrogen embrittlement of sensitized (S) and desensitized (SD) γ-stainless steels. The susceptibility to hydrogen embrittlement is expressed in terms of the ratio of reduction of areas in H_2 and He gas environments (Han et al. [59])
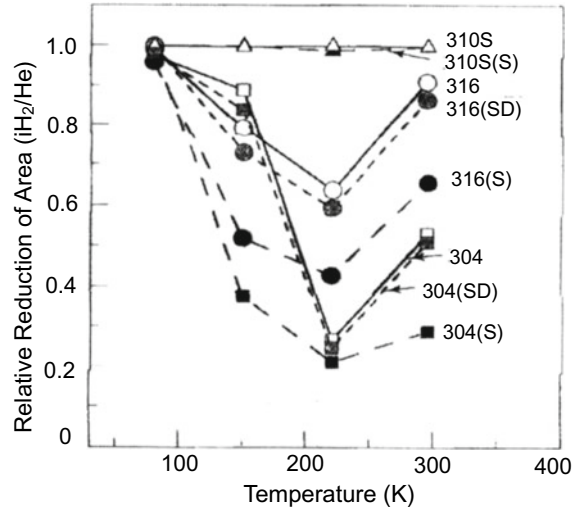
thermal hydrogen precharging to 425 at. ppm, about six times as large as the solid solubility, lowered the reduction of area from 45 to 27% and from 43 to 30% at notched-tensile tests for normal and sensitized specimens, respectively [60]. By the sensitizing heat treatment at 975 K for 15 or 300 min, the relative reductions by hydrogen were almost the same in the original and sensitized specimens. It implies no cooperative effects between hydrogen and sensitization in Type 309S.

(c)   Prestrain

Strain-induced α', highly susceptible to HE, has often been postulated to play the primary role in HE of unstable γ-stainless steel. A unique correlation between the susceptibilities to HE and the amounts of deformation-induced α' on tensile-fracture surfaces was shown for Types 304, 316, and 316L steel tested in high-pressure 90 MPa hydrogen gas at 228 ~ 358 K [61]. However, contrary findings were that the more significant amounts of α' introduced by prestraining reduced more pronouncedly slow crack growth rates for Type 301 (6 ~ 8Ni-16 ~ 18Cr) steel [62]. In the experiments, prestraining was given by rolling to a 30% reduction in thickness either at room temperature or 383 K. The amounts of α' were 57 and 0.5%, respectively, at the two temperatures. The increased amount of α' elevated the threshold stress intensity K_{TH} for the crack initiation and reduced the Stage II crack growth rate at sustained-loading tests in 108 kPa hydrogen. The results are against a common notion that α' provides a favorable crack path.

On the other hand, the suppression of martensite transformation by prestrain is well known. If the function of prestrain was to suppress microstructural alterations in the γ-phase preceding the martensite transformation, or if dislocation dynamics associated with martensite transformation, rather than martensite itself, were crucial for causing embrittlement, the reduced susceptibility by prestraining would be feasible.

Compositional effects appear in deformation microstructures and are described in Sect. 8.3.4.

8.3.3 Fractographic Features

Fractographic features of hydrogen-degraded γ-stainless steel are quite similar to those of ferritic steel stated in Sect. 7.2, such as fine dimple size on hydrogen-charged and tensile-fractured Type 309S [61] and striations on facets in transgranular fracture surfaces of severely hydrogen-charged and tensile-fractured Type 316 steel [63]. Facets containing slip lines corresponding to {111} planes were observed for hydrogen-charged and tensile-fractured Type 310S steel specimens [50]. Facets are likely due to cracking along the grain or twin boundaries. Cracks at intersections of slip bands were observed on the side surface of tensile-fractured Type 304 steel specimens containing about 10 at. ppm hydrogen [51]. Quasi-cleavage (QC) appeared at slow-elongation rate tests of Type 301 steel in 108 kPa hydrogen gas at room temperature, and the fraction of QC decreased, and fine dimples increased as the test temperature was raised [62]. Transgranular QC surfaces associated with secondary cracks were also reported on slow crack growth regions of hydrogen-charged Type 304 steel [64].

Figure 8.23 shows tensile-fracture surfaces of Type 304 steel specimens [65]. The distribution of the charged hydrogen of 30 ~ 35 mass ppm was uniform. Coarse dimples in the hydrogen-free specimen changed to a mixture of fine dimples, QC, and facets in the hydrogen-charged specimen.

Hydrogen degradation evolves even in stable Type 310 steel, as shown in Fig. 8.20, without forming α'. However, the instability of γ-stainless steel inducing the α' formation has been considered the primary cause of enhanced embrittlement.
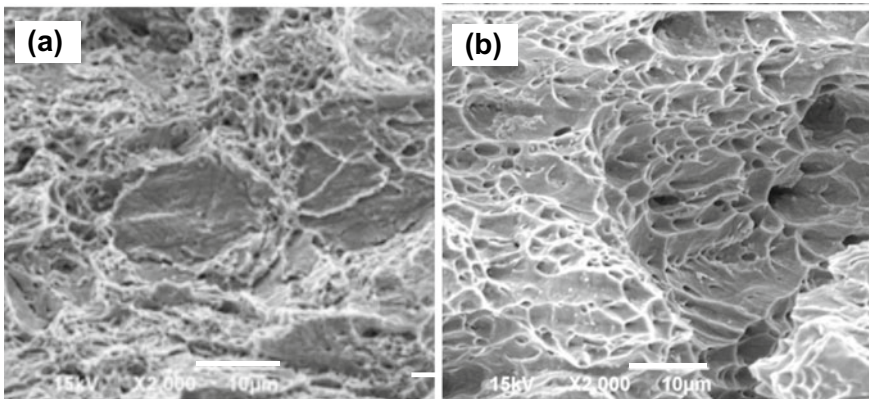

Fig. 8.23 Tensile-fracture surfaces of Type 304 stainless steel **(a)** with and **(b)** without hydrogen charging (Hatano et al. [65])

Enhanced degradation by sensitization is an example of claiming the role of α'. In fact, strain-induced α' was present along grain boundaries for sensitized Type 304. However, a substantial degradation by hydrogen still occurred in desensitized specimens, while no α' was observed at grain boundaries. It indicates that α' is not essential for the large hydrogen degradation of Type 304 at 220 K.

The fracture morphology of sensitized specimens was macroscopically IG accompanying secondary cracks vertical to the fracture surface along grain boundaries for both Types 316 and Type 304 and in both helium and hydrogen gases [59]. Close examinations of IG fracture surfaces revealed that macroscopically IG surfaces were not entirely smooth, with different morphologies depending on steel and environments. Microvoid coalescence (MVC) covered IG-like surfaces of both Type 304 and 316 when tested in helium. In hydrogen gas, dimples on IG-like surfaces of sensitized Type 304 were extremely fine, and the apparent surfaces were brittle-like.

Very fine dimples on IG surfaces are due to increased nucleation sites of fine voids. Desensitization of sensitized steels hardly changed MVC fracture morphology in helium, but it changed IG to QC in hydrogen for both Types 316 and 304. The change from MVC in helium to QC in hydrogen also appeared on transgranular fracture surfaces of solution-treated specimens. Promoting voids nucleation and their premature coalescence associated with plastic deformation is possibly the essential function of hydrogen common to both sensitized and desensitized specimens. The compositional effect is likely a matter to be examined regarding deformation microstructures in the γ-phase.

8.3.4   Deformation Microstructures

(a)   Phase changes

Besides the high susceptibility to HE of strain-induced α', deformation microstructures in the γ-phase are essential aspects for degradation. Transmission electron microscopy (TEM) is a powerful tool to reveal deformation microstructures associated with the crack propagation that constructs fracture surfaces. A high density of dislocations and the formation of ε and α' martensite were observed near the crack tip in Type 304 and Type 310 steel specimens tensile strained under cathodic hydrogen charging [56]. Increasing current densities enhanced the formation of stacking fault and ε-martensite, and the crack path was mainly along the interface between γ and ε phases. The crack propagation along the interface between γ and ε phases was also reported using high voltage TEM in Type 304 steel specimens tensile strained after cathodic hydrogen precharging [66].

As for α' produced at the transformation, a completely α-phase was shown in front of the crack tip and along the crack by Debye rings of selected area diffraction (SAD) in Type 304 steel foils tensile-fractured in an environmental cell of 108 kPa hydrogen gas [67]. The finding suggested that the α-phase was the precursor of crack extension. The difference in the SAD patterns of α' and α was not discernible, and Narita

and Birnbaum pointed out two possible hydrogen effects, increased M_d temperature favoring transformation to α' and enhanced plasticity at the crack tip. However, SAD patterns from more stable Type 310 also showed Debye rings characteristic of a very fine-grain γ-phase at the crack tip and along the crack.

(b) Strain localization

On the other hand, stacking fault and ε-martensite are sites along which strain localization and associated damage accumulation preferentially take place. Accumulation of damage is the precursor of the crack nucleation and growth as described in Sect. 7.3. Figure 8.24 [65] shows kernel average misorientation (KAM) maps obtained from electron backscatter diffraction (EBSD) for Type 304 austenitic stainless steel tensile strained to 24% at room temperature with and without gaseous hydrogen precharging under high pressure at elevated temperature. The KAM map represents orientation differences between neighboring pixels and measures the amount of strain. Blue to red colors in the KAM maps denotes five levels from 0 to 5°. The strain distribution is not uniform, and the increased areal fractions of bright (orange and red) regions imply enhanced strain localization.

The decrease in tensile ductility by hydrogen was substantial in Type 304, while Type 316L was immune to hydrogen. However, enhanced strain localization by hydrogen is present in Type 316L, though to a less extent compared to Type 304. Figure 8.25 [65] shows a quantitative comparison of strain localization in terms of area fractions of orange and red color regions for Types 304 and 316L steels strained to 24% with and without hydrogen charging. The hydrogen effect enhancing strain localization is much more distinct in Type 304 than in Type 316L. The preferential strain localization in Type 304 is due to the stacking fault energy.

Fig. 8.24 Kernel average misorientation (KAM) maps of EBSD for Type 304 austenitic stainless steels tensile strained to 24% **(a)** without and **(b)** with hydrogen precharging. Blue to red denotes higher misorientations between neighboring pixels. The arrow in **(b)** indicates annealing twin boundary (Hatano et al. [65])
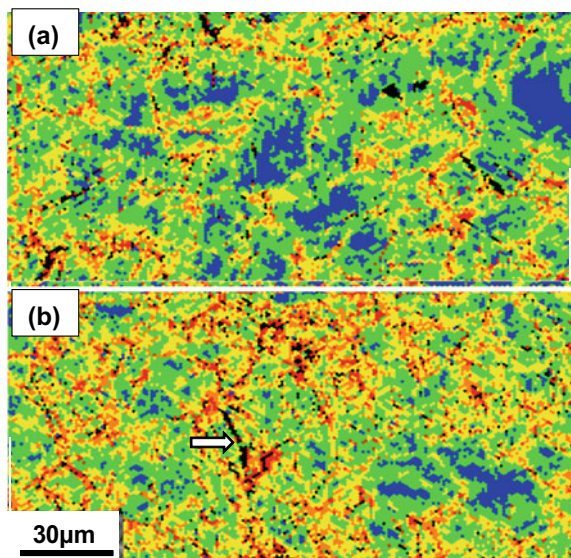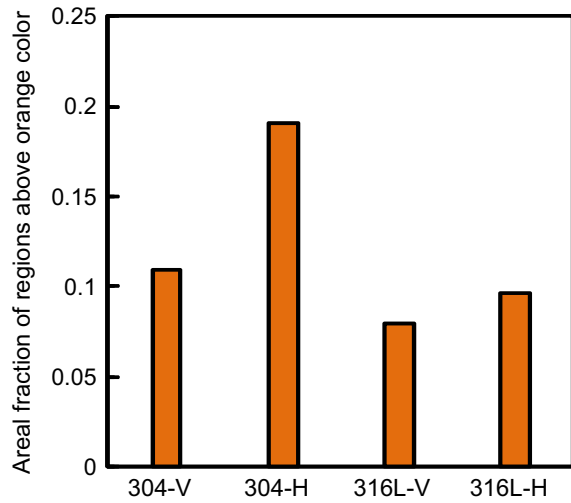
Fig. 8.25 Areal fractions of highly strained regions of orange and red colors in Fig. 7.13. Data for Type 316L are also added. Suffixes "V" and "H" denote without and with hydrogen charging, respectively (Hatano et al. [65])

The decrease in the stacking fault energy enhances strain-hardening and fractions of resultant phases, such as stacking fault and ε-martensite, act as barriers for the slip extension. High densities of fine stacking faults and streaks of ε-martensite characterize microstructures of hydrogen-charged and deformed Type 304 austenitic steel [65]. The deterioration of crystallinity associated with strain localization is described in Sect. 7.3.2.

Concurrently conducted positron annihilation spectroscopy (PAS) exhibited a more noticeable increase for Type 304 than for Type 316L in the mean positron lifetime associated with straining [65]. PAS to identify the type of hydrogen-enhanced strain-induced lattice defects is described in Sects. 3.2.2 and 7.4.1.2. Isochronal annealing of strained iron showed that the hydrogen effect on increasing positron lifetime is due to the enhanced creation of vacancies. For austenitic stainless steels, vacancy clustering proceeded more prominently in Type 304 than in Type 316L. Effects of enhanced strain localization on hydrogen embrittlement are relevant to the enhanced creation of vacancies and their clusters. Other possibilities, such as the buildup of high local hydrogen concentration, are not feasible because of the very low diffusivity of hydrogen in austenitic stainless steel. Strain-induced transformation to martensite was not detected even in a region about 0.5 mm from the fracture surface of Type 304 [65].

The strain localization was associated with the planarity of the dislocation slip and with barriers for the slip extension. TEM micrograph Fig. 8.26 [65] for hydrogen-charged Type 304 strained to 5% shows high densities of stacking faults and fine streaks of ε-martensite, as confirmed with electron microdiffraction from the red dot in Fig. 8.26(b). High dislocation densities along grain boundaries and annealing twin boundaries were also revealed. Inhomogeneous microstructures made quantitative comparisons difficult, but stacking faults, twins, and ε-martensite were observed

much more frequently in hydrogen-charged Type 304 than in Type 316L. Further, dislocation structures in Type 316L were tangled with a few stacking faults [65].

The stacking fault energy (SFE) dominates the formation of stacking fault and ε-martensite in γ-steel. The SFE of Type 304 and Type 316L estimated by a first-principles calculation [68] was about 2 and 30 mJ·m^{-2}, respectively [65]. Experimentally, the sensitization of Type 309S steel reduced SFE in the area near grain boundaries from 35 to 22 mJ·m-2 due to Cr depletion [63]. Reductions in SFE of γ-stainless steels by hydrogen are in Sect. 7.3.1. Reductions of SFE of about 20–30% by hydrogen were reported for Type 304 [56] and Type 310 [69]. The stability of γ-phase indeed originates in SFE, dominating deformation microstructures.

Plausible functions of hydrogen on the susceptibility to HE of γ-stainless steels are two-fold; one is the enhancement of strain localization through the decrease of SFE, and the other is that of the strain-induced creation of vacancies. Effects of hydrogen in various γ-stainless steel possibly originate in deformation microstructures in the γ-phase.
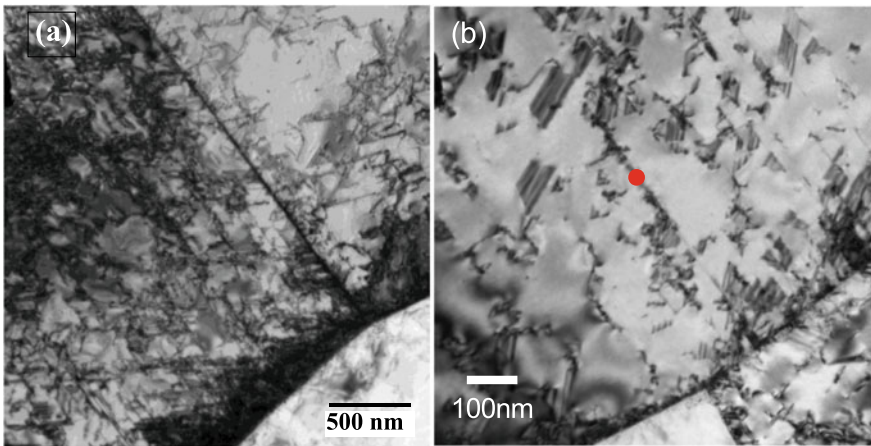

Fig. 8.26 TEM micrograph of hydrogen-charged Type 304 steel strained to 5%, showing **(a)** annealing twin band and high dislocation densities along twin and grain boundaries. Magnified view **(b)** shows high densities of stacking fault and ε-martensite (Hatano et al. [65])

References

1. N.R. Moody, S.L. Robinson, W.M. Garrison Jr., Res Mechanica **30**, 143–206 (1990)
2. I.M. Bernstein, G.M. Pressouyre, in *Hydrogen Degradation of Ferrous Alloys*, ed. by R.A. Oriani, J.P. Hirth, M. Smialowski (Noyes Pub., Park Ridge NJ, 1985), pp. 641–685
3. A. Shibata, Y. Momotani, T. Murata, T. Matsuoka, M. Tsuboi, N. Tsuji, Mater. Sci. Tech. **33**, 1524–1532 (2017)
4. W.W. Gerberich, T. Livne, X.-F. Chen, M. Kaczorowski, Metall. Trans. A **19A**, 1319–1334 (1988)
5. N. Owada, H. Majima, T. Eguchi, in *Advances in Delayed Fracture Solution*—Report of Research Group (Iron Steel Institute, Japan, 1997), pp. 111–114
6. M. Nagumo, T. Tamaoki, T. Sugawara, in *Hydrogen Effects on Materials Behavior and Corrosion Deformation Interactions*, ed. by N.R. Moody, A.W. Thompson, R.E. Ricker, C.W. Was, K.H. Jones (TMS, Warrendale PA, 2003), pp. 999–1008
7. H.K.D.H. Bhadesia, in *Bainite in Steels*, 2nd edn (The Institute of Materials, London, 2001)
8. F. Nakasato, F. Terasaki, Tetsu-to-Hagané **61**, 856–868 (1975)
9. I.-G. Park, A.W. Thompson, Metall. Trans. A, **21A**, 465–477 (1990)
10. R.A. Oriani, P.H. Josephic, Scr. Metall. **13**, 469–471 (1979)
11. J.C. Charbonnier, H. Margot-Marette, A.M. Brass, M. Aucouturier, Metall. Trans. A **16A**, 935–944 (1985)
12. S. Yamazaki, T. Takahashi, Tetsu-to-Hagané **83**, 454–459 (1997)
13. T. Tsuchida, T. Hara, K. Tsuzaki, Tetsu-to-Hagané **88**, 771–778 (2002)
14. J.F. Lessar, W.W. Gerberich, Metall. Trans. A **7A**, 953–960 (1976)
15. N.R. Moody, R.E. Stoltz, M.W. Perra, Scr. Metall. **20**, 119–122 (1985)
16. J. Kameda, Acta Metall. **34**, 1721–1735 (1986)
17. S.K. Banerji, C.J. McMahon Jr., H.C. Feng, Metall. Trans. A **9A**, 237–247 (1978)
18. H. Asahi, Y. Sogo, M. Ueno, H. Higashiyama, Corrosion **45**, 519–527 (1989)
19. H. Fuchigami, H. Minami, M. Nagumo, Phil. Mag. Lett. **86**, 21–29 (2006)
20. C.J. McMahon Jr., Eng. Fract. Mech. **68**, 773–788 (2001)
21. K. Yoshino, C.J. McMahon, Metall. Trans. **5**, 363–370 (1974)
22. J. Kameda, C.J. McMahon Jr., Metall. Trans. A **14A**, 903–911 (1983)
23. J. Watanabe, K. Takai, M. Nagumo, Tetsu-to-Hagané **82**, 947–952 (1996)
24. Y. Takeda, C.J. McMahon Jr., Metall. Trans. A **12A**, 1255–1266 (1981)
25. N. Bandyopadhyay, J. Kameda, C.J. McMahon Jr., Metall. Trans. A **14A**, 881–888 (1983)
26. M. Nagumo, H. Matsuda, Phil. Mag. A **82**, 3415–3425 (2002)
27. T. Inoue, K. Yamamoto, M. Nagumo, in *Hydrogen Effects in Metals*, ed. by I.M. Bernstein, A.W. Thompson (Metallurgical Society of AIME, Warrendale PA, 1981), pp. 777–784
28. T. Inoue, K. Yamamoto, M. Nagumo, K. Miyamoto, in *Hydrogen in Metals*, Proceedings of 2nd International Symposium, Supplement of Transactions of Japan Institute of Metals, vol 21 (1980), pp. 433–436
29. Y.H. Kim, J.W. Morris Jr., Metall. Trans. A **14A**, 1883–1888 (1983)
30. A. Shibata, H. Takahashi, N. Tsuji, ISIJ Int **52**, 208–212 (2012)
31. A. Shibata, T. Murata, H. Takahashi, T. Matsuoka, N. Tsuji, Metall. Mater. Trans. A **46A**, 5685–5696 (2015)
32. A. Shibata, T. Matsuoka, A. Ueno, N. Tsuj, Int J Fract **205**, 73–82 (2017)
33. T. Kobayashi, D.A. Shockey, Eng. Fract. Mech. **77**, 2370–2384 (2010)
34. M. Michiuchi, S. Nambu, Y. Ishimoto, J. Inoue, T. Koseki, Acta Mater. **57**, 5283–5291 (2009)
35. T. Depover, D. Pérez Escobar, E. Wallaert, Z. Zermout, K. Verbeken, Int. J. Hydrogen Energy **39**, 4647–4656 (2014)
36. Q. Liu, Q. Zhou, J. Venezuela, M. Zhang, A. Atrens, Corros. Sci. **125**, 114–138 (2017)
37. R.G. Davies, Metall. Trans. A **12A**, 1667–1672 (1981)
38. R.G. Davies, Scr. Metall. **17**, 889–892 (1983)
39. M. Koyama, C.C. Tasan, E. Akiyama. K. Tsuzaki, D. Raabe, Acta Mater. **70**, 174–187 (2014)

40. K. Takashima, Y. Yoshikawa, K. Yokoyama, Y. Funakawa, ISIJ Int. **58**, 173–178 (2018)
41. J.L. Gu, K.D. Chang, H.S. Fang, B.Z. Bai, ISIJ Int. **42**, 1560–1564 (2002)
42. S.L.I. Chan, H.L. Lee, J.R. Yang, Met Trans A **22A**, 2579–2586 (1991)
43. R. Petrov, L. Kestens, A. Wasilkowska, Y. Houbaert, Mater. Sci. Eng. A **447**, 285–297 (2007)
44. S.J. Kim, D.W. Yun, D.W. Suh, K.Y. Kim, Electrochem. Comm **24**, 112–115 (2012)
45. D.P. Escobar, T. Depover, L. Duprez, K. Verbeken, M. Verhaege, Acta Mater. **60**, 2593–2605 (2012)
46. J. Speer, D.K. Matlock, B.C. De Cooman, J.G. Schroth, Acta Mater. **51**, 2611–2622 (2003)
47. J. Yang, F. Huang, Z. Guo, Y. Rong, N. Chen, Mater. Sci. Eng. A **665**, 76–85 (2016)
48. J. Kobayashi, R. Sakata, N. Kakefuda, G. Itoh, T. Hojo, ISIJ Int. **61**, 1315–1321 (2021)
49. K. Farrell, M.B. Lewis, Scr. Metall. **15**, 661–664 (1981)
50. A. Szummer, in *Hydrogen Degradation of Ferrous Alloys*, ed. by R.A. Oriani, J.P. Hirth, M. Smialowski (Noyes Pub., Park Ridge NJ, 1985), pp. 512–534
51. K. Kamachi, Trans. ISIJ **18**, 485–491 (1978)
52. D.G. Ulmer, C.J. Altstetter, Acta Metall. Mater. **41**, 2235–2241 (1993)
53. N. Narita, C.J. Altstetter, H.K. Birnbaum, Metall. Trans. A **13A**, 1355–1365 (1982)
54. K.J.L. Iyer, Scr. Metall. **6**, 721–726 (1972)
55. A.W. Thompson, O. Buck, Metall. Trans. A **7A**, 329–331 (1976)
56. A. Inoue, Y. Hosoya, T. Masumoto, Trans. ISIJ **19**, 171–178 (1979)
57. G.R. Caskey, Jr., in *Hydrogen Degradation of Ferrous Alloys*, ed. by R.A. Oriani, J.P. Hirth, M. Smialowski (Noyes Pub., Park Ridge NJ, 1985), pp. 822–862
58. S. Singh, C. Altstetter, Metall. Trans. A **13A**, 1799–1808 (1982)
59. G. Han, J. He, S. Fukuyama, K. Yokogawa, Acta Mater. **46**, 4559–4570 (1998)
60. A.W. Thompson, Mater. Sci. Eng. **14**, 253–264 (1974)
61. T. Omura, M. Miyahara, H. Senba, M. Igarashi, H. Hirata, J. High Pressure Inst. Jpn. **46**, 205–213 (2008)
62. T.-P. Perng, C.J. Altstetter, Metall. Trans. A, **19A**, 145–152 (1988)
63. H. Hänninen, T. Hakkarainen, Metall. Trans. A **10A**, 1196–1199 (1979)
64. C.L. Briant, Metall. Trans. A **10A**, 181–189 (1979)
65. M. Hatano, M. Fujinami, K. Arai, H. Fujii, M. Nagumo, Acta Mater. **67**, 342–353 (2014)
66. T. Nakayama, M. Takano, Corrosion-NACE **38**, 1–9 (1982)
67. N. Narita, H.K. Birnbaum, Scr. Metall. **14**, 1355–1358 (1980)
68. L. Vitos, J.-O. Nilson, B. Johansson, Acta Mater. **54**, 3821–3826 (2006)
69. P.J. Ferreira, I.M. Robertson, H.K. Birnbaum, Mater. Sci. Eng. **207–209**, 93–96 (1996)